AGU PUBLICATIONS

Space Weather

RESEARCH ARTICLE

10.1002/2017SW001695

SWMF Global Magnetosphere Simulations of January 2005: Geomagnetic Indices and Cross-Polar Cap Potential

John D. Haiducek[1], **Daniel T. Welling**[1], **Natalia Y. Ganushkina**[1,2], **Steven K. Morley**[3], **and Dogacan Su Ozturk**[1]

[1]Climate and Space Sciences, University of Michigan, Ann Arbor, MI, USA, [2]Finnish Meteorological Institute, Helsinki, Finland, [3]Space Science and Applications Group (ISR-1), Los Alamos National Laboratory, Los Alamos, NM, USA

Abstract We simulated the entire month of January 2005 using the Space Weather Modeling Framework (SWMF) with observed solar wind data as input. We conducted this simulation with and without an inner magnetosphere model and tested two different grid resolutions. We evaluated the model's accuracy in predicting *Kp*, *SYM-H*, *AL*, and cross-polar cap potential (CPCP). We find that the model does an excellent job of predicting the *SYM-H* index, with a root-mean-square error (RMSE) of 17–18 nT. *Kp* is predicted well during storm time conditions but overpredicted during quiet times by a margin of 1 to 1.7 *Kp* units. *AL* is predicted reasonably well on average, with an RMSE of 230–270 nT. However, the model reaches the largest negative *AL* values significantly less often than the observations. The model tended to overpredict CPCP, with RMSE values on the order of 46–48 kV. We found the results to be insensitive to grid resolution, with the exception of the rate of occurrence for strongly negative *AL* values. The use of the inner magnetosphere component, however, affected results significantly, with all quantities except CPCP improved notably when the inner magnetosphere model was on.

Key Points:

- Increasing grid resolution from that used by SWPC improves *AL* prediction during disturbances but has little effect on *Kp*, *SYM-H*, or CPCP
- The model does an excellent job at predicting *SYM-H* but less well in predicting *AL*
- SWMF tends to overpredict *Kp* and CPCP during quiet times but predicts those quantities better during active times

Supporting Information:

- Supporting Information S1
- Data Set S1

Correspondence to:
J. D. Haiducek,
jhaiduce@umich.edu

Citation:
Haiducek, J. D., Welling, D. T., Ganushkina, N. Y., Morley, S. K., & Ozturk, D. S. (2017). SWMF global magnetosphere simulations of January 2005: Geomagnetic indices and cross-polar cap potential. *Space Weather*, *15*, 1567–1587. https://doi.org/10.1002/2017SW001695

Received 23 JUL 2017
Accepted 24 OCT 2017
Accepted article online 30 OCT 2017
Published online 4 DEC 2017

1. Introduction

Magnetohydrodynamic (MHD) models (e.g., De Zeeuw et al., 2000; Lyon et al., 2004), coupled with inner magnetosphere and ionosphere models (e.g., Cramer et al., 2017; Glocer et al., 2012; Pembroke et al., 2012; Yu et al., 2014), are a powerful tool for understanding the dynamics of the Earth's magnetosphere (e.g., Crooker et al., 1998; Zhang et al., 2007). By solving a subset of Maxwell's equations, an MHD solver provides magnetic fields and current systems throughout its computational domain. Coupling the MHD model to an inner magnetosphere and ionosphere model produces a system that accounts for ring currents and ionospheric currents as well. This results in a detailed representation of magnetospheric dynamics that is applicable under a wide variety of conditions.

These capabilities naturally make the coupled global MHD and ring current approach attractive for forecasting applications. In 2016 the NOAA Space Weather Prediction Center (SWPC) added a geospace modeling capability based on the Space Weather Modeling Framework (SWMF) (Tóth et al., 2005, 2012) to their suite of operational forecasting tools (http://clasp.engin.umich.edu/articles/view/715). This was the result of a community validation effort focusing on six storm events, in which three MHD models and two empirical models were evaluated with respect to their ability to predict $\frac{dB}{dt}$ at several ground-based magnetometer stations. The validation effort is described in Pulkkinen et al. (2013) and builds from Pulkkinen et al. (2010) and Rastätter et al. (2011). Pulkkinen et al. (2013) found that the SWMF achieved the best predictive skill of the models evaluated, but with the caveat that the predictions delivered by SWMF may not be adequate for some operational uses. A number of follow-up papers have examined the results of this effort further. Glocer et al. (2016) evaluated the models' ability to reproduce the local *K* index, finding that the SWMF performed especially well in predicting local *K*. Welling et al. (2017) showed that the SWPC events exceeded the range of validity for the empirical ionospheric conductance models used in the participating MHD codes, and that all of the models tended to underpredict surface $\frac{dB}{dt}$, though SWMF less so than the others. Anderson et al. (2017) compared the field-aligned currents from the models with those obtained using the Active Magnetosphere and Planetary Electrodynamics Response Experiment.

Though unique in its rigorous comparison of multiple models, the scope of Pulkkinen et al. (2013) was limited to a small number of storm events. This has been a common practice within the MHD modeling community in recent years. Simulations of single storm events constitute a majority of existing MHD papers. Some representative examples include Raeder et al. (2001), which simulated the 14–16 July 2001 "Bastille Day" storm, Palmroth et al. (2003), which simulated a major storm from 6 to 7 April 2000, Lopez et al. (2001), which simulated a March 1995 substorm and a January 1997 storm, and Kress et al. (2007), which shows MHD and particle tracing results for the 29 October 2003 storm. MHD models have also been used to study hypothetical extreme events to better understand the possible effects of such events. For instance, Groth et al. (2000) simulated a coronal mass ejection (CME) from the Sun and the resulting effects on Earth, Ngwira et al. (2013) simulated the effects of a hypothetical "Carrington-type" space weather event, and Ngwira et al. (2014) presented simulations aimed at predicting the effects of the 23 July 2012 CME if it had been directed earthward.

MHD models have been used to study quiet time conditions as well. Early work such as Wu et al. (1981) and Ogino et al. (1992) simulated steady solar wind conditions, while Raeder et al. (1998) modeled time-dependent quiet time conditions. Some more recent work such as Welling and Ridley (2010) has included quiet time periods, although that paper focused primarily on storms. However, these constitute a minority of papers in recent years, and like the storm papers, they tend to cover short periods of time.

Only a few papers to date describe MHD simulations more than a few days in duration. Guild et al. (2008) compared in situ plasma sheet observations with MHD output from a 2 month simulation, finding the model generally able to reproduce the gross features of the plasma sheet in a statistical sense. Zhang et al. (2011) analyzed the field-aligned current structures and polar cap potentials from the Guild et al. (2008) simulations, finding a significant underprediction of current strength and overprediction of CPCP. Huang et al. (2010) found an MHD code to be capable of reproducing the statistics of ULF waves in geosynchronous orbit over a 27 day simulation. Juusola et al. (2014) compared MHD-derived CPCP and auroral index predictions with observations for a 1 year period using Facskó et al.'s (2016) 1 year global MHD simulation. That work was accomplished using a large number of short simulations run independently of each other, because the Grand Unified Magnetosphere-Ionosphere Coupling Simulation (GUMICS-4) developed by Janhunen et al. (2012) is a single core code. This way the simulation state was effectively reinitialized approximately every 5 h. Facskó et al.'s (2016) simulations were unsuccessful at reproducing a number of aspects of the auroral oval structures and obtained ground magnetic field perturbations that were weaker than observed by at least a factor of 5 (Juusola et al., 2014). Facskó et al. (2016) derived the magnetic footprints by magnetic field mapping from the Cluster SC3 using the GUMICS simulation and also using the Tsyganenko (T96) model in order to compare two methods. The study showed that the footprints determined using the GUMICS simulation agreed relatively well with the T96 empirical model; however, the footprints agreed better in the Northern Hemisphere than the Southern one during quiet conditions. Wiltberger et al. (2017) cover a period of nearly a month (20 March to 16 April 2008), which was chosen because it contains a wide variety of solar wind conditions but no major geomagnetic storms. The results presented in Wiltberger et al. (2017) focused on field-aligned currents and cross-polar cap potential (CPCP), finding that the simulations reproduced the statistical features of the observed field-aligned current patterns but tended to produce weaker field-aligned currents and higher potentials than the Weimer05 empirical model.

Some focus on storms is no doubt appropriate due to the hazards posed by such events. However, the approach of manually selecting storm events to validate a model can be problematic. Manual selection of storm events can introduce biases since the particular storms chosen may not be representative examples. Furthermore, undue focus of validation efforts on strong storm events could result in a model that is optimized for such events at the expense of moderately disturbed or quiet conditions. This can potentially undermine the model's usefulness as a forecasting tool, since a model designed only to model storms could overpredict or underpredict activity in weakly or moderately disturbed conditions. In the case of overprediction, this could lead to an elevated false alarm rate for storm conditions. In the case of underprediction, it could lead to potentially significant activity being missed. In either case, it could erode confidence in the model on the part of forecasters and customers if the model appears to be useful only during times of strong activity.

If a model performs poorly during quiet time conditions, this could be symptomatic of problems that persist during disturbed periods as well. Small deficiencies in a model may in some cases be apparent during quiet time but be difficult to notice during storm time. In addition, quiet time conditions just prior to a storm may subtly affect the dynamics of the storm itself. Therefore, improvements to a model's representation of the quiet time magnetosphere are likely to improve its representation of storm time dynamics as well.

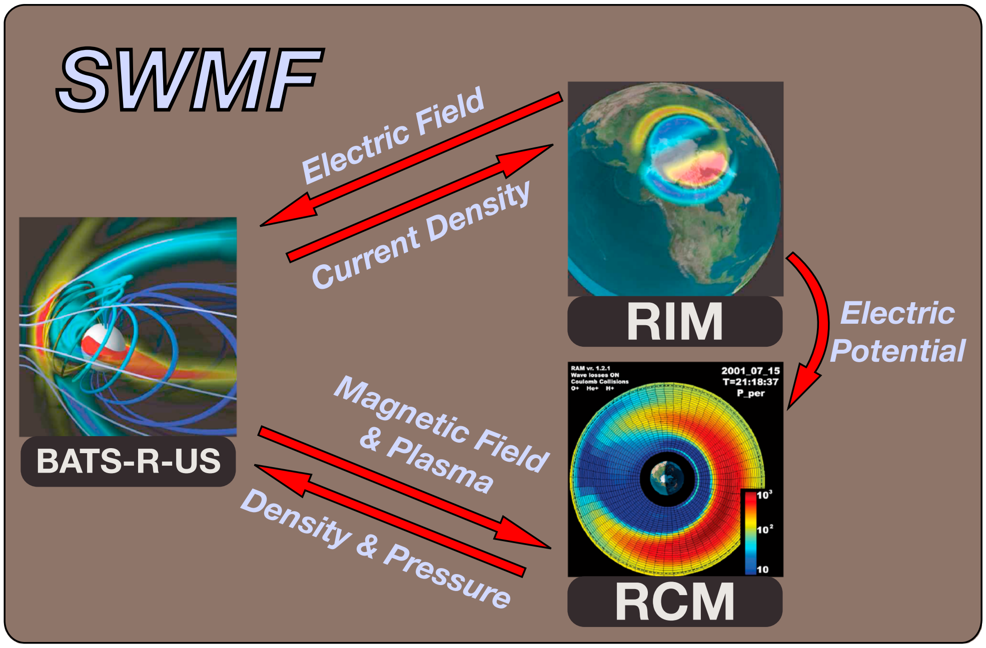

Figure 1. Illustration of the models (components within SWMF) and couplings in use. Arrows denote the information that is passed between the components.

In the present work, we investigate the capability of the SWMF to deliver accurate predictions of geomagnetic indices and cross-polar cap potential. We include a realistic mix of quiet and disturbed conditions by studying the entire 1 month period of January 2005, rather than a set of selected events. In addition, the use of a single continuous time period for validation reduces any errors caused by a poor initial condition (provided those errors dissipate over time). Finally, the use of a single continuous run is more representative of operational forecasting usage, in which a continuous stream of real-time data is fed into the model.

We drive three different configurations of the SWMF (the details of which are described in section 2.1) with solar wind data observed by the Advanced Composition Explorer (ACE) spacecraft. The model's input data are described in more detail in section 2.2. The model provides magnetic field values at a number of ground stations. From these we calculate values of the geomagnetic indices *SYM-H*, *Kp*, and *AL*, as well as CPCP. *SYM-H* is the longitudinally symmetric northward component of six low-latitude magnetometers, typically regarded as a measure of ring current and other current systems. *Kp* (planetarische Kenziffer) is an index computed from a number of mostly midlatitude magnetometers and is typically regarded as a general measure of global geomagnetic activity. *AL* (auroral lower) is computed from the most negative northward component of a set of auroral magnetometers and is regarded as a measure of auroral zone currents, primarily the westward electrojet. Cross-polar cap potential (CPCP) is the difference between the minimum and maximum electrostatic potential over the polar cap and provides an indication of the coupling strength between the solar wind and the magnetosphere. Details on each of these quantities are given in section 2.3.

After obtaining observed values for the indices and calculating equivalent values from the model, we calculate metrics to measure each model configuration's ability to predict each geomagnetic index and, from these, identify strengths and weaknesses of each model configuration. The specific metrics are described in section 2.4. Results for each geomagnetic index are presented and discussed in section 3, and conclusions are given in section 5.

2. Methodology

2.1. Model Description

The model we use consists of the BATS-R-US (Block-Adaptive-Tree Solar Wind, Roe-Type Upwind Scheme), coupled to the Rice Convection Model (RCM) and the Ridley Ionosphere Model (RIM). A schematic of the coupling is shown in Figure 1. BATS-R-US, described in Powell et al. (1999) and De Zeeuw et al. (2000), is an adaptive

Table 1
Summary of the Model Configurations Used

Name	Grid	RCM	Composition model
SWPC	SWPC	Y	Fixed
Hi-res w/ RCM	Hi-res	Y	Young et al. (1982)
Hi-res w/o RCM	Hi-res	N	Fixed

mesh MHD solver that solves the ideal MHD equations throughout the magnetosphere. RCM (Sazykin, 2000; Toffoletto et al., 2003; Wolf et al., 1982) models the inner magnetosphere, and RIM (Ridley et al., 2003; 2004a) simulates ionospheric electrodynamics. Coupling is accomplished using SWMF. Couplings between the models are identified by arrows in Figure 1, which point in the direction of information flow and are labeled with the quantities passed between the models. The couplings are as follows.

1. BATS-R-US MHD delivers magnetic field and plasma moments to RCM.
2. RCM provides plasma density and pressure to BATS-R-US.
3. BATS-R-US sends current density to RIM.
4. RIM delivers electric field to BATS-R-US.
5. RIM delivers electric potential to RCM.

This combination of models and couplings is currently being used for operational forecasting of $\frac{dB}{dt}$, *Dst*, and *Kp* at the Space Weather Prediction Center (SWPC).

We run the model in three different configurations, summarized in Table 1. The SWPC configuration is nearly identical to that used operationally by SWPC (the main differences, besides the input data being historical rather than real time, being in what output files are written during the run). The other configurations are similar but use a higher-resolution grid and other modifications. The two grids that are used are described in detail in section A1. The switch to the higher-resolution grid necessitated other modifications in order to maintain the model's performance with respect to *SYM-H*. First, the plasma sheet O/H mass density ratio (used in coupling between BATS-R-US and RCM) is determined adaptively based on the current values of $F_{10.7}$ flux and *Kp* index using the empirical model from Young et al. (1982), rather than using a fixed ratio as is used in the SWPC configuration. Second, a boundary condition parameter that controls how much the inner boundary density increases as cross-polar cap potential increases (described in Pulkkinen et al., 2013) was reduced from 0.1 to 0.08. These changes result in *SYM-H* predictions that are similar to the SWPC configuration and have minimal effect on the other quantities analyzed in this paper. Details of the model configuration, including settings for each component, are described in Appendix A.

2.2. Model Execution

In order to create a data set for statistical evaluation of the model, we ran the model for the entire month of January 2005. We repeated this for each of the three configurations described in section 2 of this paper. This time period was selected to support a project currently in progress to evaluate the model's capability to predict magnetospheric substorms. Sequences of substorms in January 2005 were previously studied in Morley (2007) and Morley et al. (2009), and the period was identified as having a sufficiently large number of substorms to allow statistical analysis with regard to substorm predictions. The month was in the late declining phase of solar cycle 23. Minima, maxima, and medians of observed quantities characterizing the month are shown in Table 2. The month includes three geomagnetic storms. The first, on 7 January, was the result of a coronal mass ejection (CME) indicated by a small velocity change but a large spike in proton density. The 7 January storm reached a minimum *SYM-H* of −112 nT. The second storm, on 16 January, was the result of a CME indicated by a solar wind velocity increase from 600 to 800 km/s and a large density spike. An additional CME arrived on 18 January, before the completion of recovery from the 16 January storm. The 16 January storm reached a minimum *SYM-H* of −107 nT. The third storm was on 21 January. The 21 January storm was the result of a CME that resulted in a solar wind speed increase from 600 to 900 km/s and a large density spike. The 21 January storm reached a minimum *SYM-H* of −101 nT. A final CME arrived on 31 January but did not result in a geomagnetic storm.

To simulate this month, we drive the model using solar wind velocity, magnetic field, density, and temperature, which are used to construct the upstream boundary condition of BATS-R-US. The only other input parameter is $F_{10.7}$ flux, which is used by RIM in computing ionospheric conductivity (Moen & Brekke, 1993; Ridley et al., 2004b). In the high-resolution configuration with RCM, $F_{10.7}$ is also used to compute the oxygen to hydrogen ratio via the Young et al. (1982) empirical model.

Solar wind parameters are obtained from the 1 min OMNI data set provided by the NASA Goddard Spaceflight Center (GSFC). This is a combined data set that includes data from multiple spacecraft, although during the time period in question the data came primarily from the ACE spacecraft. The OMNI date is provided

Table 2
Minimum, 25th Percentile, Median, 75th Percentile, and Maximum for a Number of Observed Quantities Characterizing the Solar Wind Conditions and (Observed) Geomagnetic Conditions During the Month of January 2005

	Min	25th percentile	Median	75th percentile	Max
IMF B_z (nT)	−27.97	−1.7	0.28	2.83	30.92
Solar wind u_x (km/s)	318	468	570	672	1055
Solar wind dynamic pressure (nPa)	0.0859	1.53	2.07	3.03	80.62
Kp	0.0	2.0	3.0	4.0	8.0
SYM-H (nT)	−112	−29	−17	−7	57
AL (nT)	−4,418	−279	−123	−40	10
CPCP (kV)	6.67	27.0	63.2	77.5	1,460

Note. Components of interplanetary magnetic field (IMF) and solar wind velocity are given in GSM coordinates.

"time shifted" to the bow shock nose using the techniques described in Weimer and King (2008). We obtain $F_{10.7}$ observations from http://lasp.colorado.edu/lisird/tss/noaa_radio_flux.html, that combine the historical archive available through the National Centers for Environmental Information with modern measurements managed by NOAA SWPC. The flux values are the 1 AU adjusted flux observed at Penticton, BC (Tapping, 2013).

The solar wind data receives some additional processing before being input to the model. In addition to the OMNI data, we use temperatures from the ACE spacecraft, time-shifted by 45 min. To simplify some of the postprocessing and analysis, only the *x* component of velocity was used and the *y* and *z* components were set to zero. This reduces the motion of the magnetotail so that it remains near the *x* axis of the grid. Although the *y* and *z* components can significantly affect the orientation of the magnetotail, we expect they would have relatively little impact on the geomagnetic indices that are the focus of the present work (see, e.g., Borovsky, 2012). The *x* component of the interplanetary magnetic field (IMF) was also set to zero in order to reduce the divergence of the magnetic field in the simulation.

Gaps of less than 1 h in the OMNI data are filled by linear interpolation. Three gaps of longer duration had to be filled in from other sources. The first of these was on 18 January from 06:11 to 13:52 UT, the second was from 7:14 UT on 20 January to 21:44 on 21 January, and the third was from 01:04 to 09:13 UT on 22 January. These were due to instrument problems that occurred with the Solar Wind Electron, Proton, and Alpha Monitor (SWEPAM) instrument on the ACE satellite in its default mode, which attempts to track the solar wind peak in energy. SWEPAM operates in a second mode approximately once every 0.5 h, which samples most of the instrument's energy range rather than just the peak (McComas et al., 1998). The data from this secondary mode was used for solar wind density, temperature, and velocity during the gaps in the OMNI data set. Magnetic fields for the gap periods were available at a 1 min cadence from the ACE Level 2 data.

Since the ACE spacecraft is located well beyond the upstream boundary of the model, it must be propagated to the upstream boundary in some way. The data obtained from OMNI are provided already time shifted to the bow shock nose and were used as is (see https://omniweb.gsfc.nasa.gov/html/HROdocum.html for a description of the time shifting algorithm). The ACE SWEPAM data used to fill the gaps on 18–22 January were propagated to the upstream boundary by solving a system of 1-D advection equations:

$$\frac{\partial q_i}{\partial t} = u_x \frac{\partial q_i}{\partial x}. \tag{1}$$

Here q_i denotes one of the solar parameters, and u_x denotes the solar wind velocity in the *x* direction. The "time shifting" method used to create the OMNI data set (similar techniques are described in a number of papers such as Cash et al., 2016 and Weimer et al., 2003, 2004) is equivalent to solving equation (1) using the method of characteristics.

In the present work we solve the advection equation using a second-order finite volume method with a min-mod limiter and explicit Euler time integration on an evenly spaced 1,000-point grid. The time step is adjusted dynamically to maintain a maximum Courant-Friedrichs-Lewy number of 0.5. The particulars of this class of numerical schemes are described in a number of references such as Hirsch (2007).

Once the runs are completed, we evaluate the model configurations with regard to their ability to predict *Kp*, *SYM-H*, *AL*, and CPCP. Observational data for the *Kp* index was provided by the NOAA National Geophysical

Data Center (NGDC) and was obtained through the NASA/GSFC 1 h OMNI data set. Observational data for the *SYM-H* index provided by World Data Center Kyoto was obtained through the NASA/GSFC 1 min OMNI data set. Magnetic fields at ground-based magnetometer stations were obtained from SuperMAG (http://supermag.jhuapl.edu/Gjerloev, 2012) and used to calculate the *AL* index as described in section 2.3. Since no direct observation of CPCP is available, we instead use the Assimilative Mapping of Ionospheric Electrodynamics (AMIE) model, which estimates CPCP based on a number of observational data sets (Richmond, 1992; Richmond & Kamide, 1988). The SpacePy python library (Morley et al., 2011, 2014) was used for a number of tasks including reading the MHD output and some of the observational data sets.

2.3. Predicted Quantities Assessed

The observed quantities assessed in this paper are all derived from ground-based magnetometers. In order to reproduce these observations with the MHD model, the magnetic fields resulting from magnetospheric and ionospheric currents are calculated at various points on the Earth's surface. This is accomplished using a Biot-Savart integral over the entire MHD domain, as well as the height-integrated Hall and Pedersen currents computed by RIM (Yu & Ridley, 2008; Yu et al., 2010). From these magnetic fields we obtain equivalents to the geomagnetic indices *Kp*, *SYM-H*, and *AL*.

The *Kp* index is a measure of general geomagnetic activity and is particularly sensitive to magnetospheric convection and to the latitude of the auroral currents (Thomsen, 2004). *Kp* is calculated from 13 magnetometer stations whose geomagnetic latitudes range from 54 to 63° (Rostoker, 1972). *Kp* is obtained from the local *K* (Kenziffer) index that is calculated individually for each magnetometer. The procedure for calculating local *K* is described in Bartels et al. (1939), and the procedure for calculating the planetary *Kp* from local *K* is given in Mayaud (1980). *Kp* has historically been reported with fractional values denoted with "+" and "−" symbols, with, e.g., 4+ indicating $4\frac{1}{3}$ and 4− indicating $3\frac{2}{3}$. Since the "+" and "−" notation would complicate presentation and analysis, we follow the convention used in the OMNI data set where the fractional components are rounded to the nearest tenth, i.e., "4−"= 3.7 and "4+"= 4.3.

Although the model *Kp* could be computed using the model output for the 13 stations used observationally, we instead use a different set of locations. These consist of an evenly spaced ring of 24 points having a constant latitude of 60°. For each of the 24 points, the local *K* value is calculated using the procedure described in Bartels et al. (1939). The *K*-scale mapping for the magnetometer station Niemegk (also given in Bartels et al., 1939) is applied to all stations. This choice of mapping was found by trial and error to produce the best *Kp* predictions. Having obtained the local *K* values for each of the 24 points, the *Kp* index is then computed as the mean of these local *K* values, rounded to the nearest one third. Rather than calculating the model *Kp* every 3 h as is done in the observations, the model *Kp* is calculated using a rolling 3 h window, and values are output every minute. This rolling 3 h window ends at the time of each output, so that at the time of the observations the model's rolling window coincides with the period used to calculate the observed *Kp*.

The *AL* index, introduced in Davis and Sugiura (1966), provides a measure of the effect of the westward electrojet on the surface magnetic field. While Davis and Sugiura (1966) used a set of 10 magnetometer stations, we calculate the *AL* index from an alternate set of magnetometers, the complete list of which is provided in the supporting information. An identical set of magnetometer locations is used in both the model and observations. Since the Biot-Savart integrals used in the model explicitly exclude the intrinsic field of the Earth, the baseline removal step described in Davis and Sugiura (1966) is not necessary for the model output. For the observational data, we use data from SuperMAG that has the baseline signal removed according to the procedures described in Gjerloev (2012). The remainder of the *AL* calculation procedure (following baseline removal) is the same for both model and observations and is implemented as described in Davis and Sugiura (1966).

The *SYM-H* index is intended to measure the strength of currents circling the Earth around the dipole axis. It is calculated from a set of near-equatorial magnetometers according to procedures described in Iyemori (1990) and http://wdc.kugi.kyoto-u.ac.jp/aeasy/asy.pdf. *SYM-H* is often described as a measure of the symmetric ring current. However, it was shown (see the review by Maltsev, 2004, and references therein) that it contains contributions from many other current systems (magnetopause currents, cross-tail current, partial ring current, and substorm current wedge), and their contributions can be significant or even dominant during disturbed conditions (e.g., Dubyagin et al., 2014; Ganushkina et al., 2004; Liemohn et al., 2001; Kalegaev et al., 2005; Ohtani et al., 2001). *SYM-H* is very similar to the *Dst* index, differing primarily in that *SYM-H* uses a larger number of magnetometer stations and is calculated at a higher time resolution. Wanliss and Showalter (2006) showed that despite the differences in how *SYM-H* and *Dst* are calculated, *SYM-H* can effectively be used as a high-resolution substitute for *Dst*. Katus and Liemohn (2013) found that the difference (measured in RMSE) between *SYM-H* and *Dst* was 9.1 nT during the period 1985–2005. During the same interval, the RMSE difference between *SYM-H* and USGS *Dst* (a 1 min cadence *Dst* implementation provided by the U.S. Geological Survey, described in Gannon and Love, 2011) was 11.0 nT. Since these very similar indices differ from each other on the scale of 9–11 nT, one could consider model predictions of *SYM-H* with errors less than 9–11 nT to be indistinguishable from observations.

As with *Kp*, SWMF provides output for *SYM-H*. Rather than calculating *SYM-H* using the set of surface magnetometers used in the observations, SWMF calculates the magnetic perturbation in the direction of the magnetic pole via a Biot-Savart integration of all currents within the MHD domain about a point at the center of the Earth. Since the magnetic field is calculated at the center of the Earth, the step of averaging in longitude described in Iyemori (1990) is not needed. This methodology was validated against storm time observations in Rastätter et al. (2011).

Cross-polar cap potential (CPCP) is the difference between the maximum and minimum electric potential over the polar cap. It is dependent on the solar wind electric field, the size of the open flux region connecting the polar cap to the magnetopause, and the magnetospheric dynamics that determine the strength of the coupling between those two regions (Bristow et al., 2004; Lockwood & Morley, 2004; Milan, 2004). Observationally, CPCP must be obtained indirectly, and for the present work we used output from the AMIE model (Richmond, 1992; Richmond & Kamide, 1988), which computes a potential pattern through an expansion of basis functions chosen by fitting to observations from magnetometers, radar, and spacecraft. CPCP in the model is obtained from the potentials computed by the RIM ionosphere model.

2.4. Assessing Prediction Quality

To give an overall picture of the model's agreement with the observations, we calculate accuracy and bias metrics for the entire month, as well as probability distributions, for each predicted quantity. Given a set of observations x_i and corresponding predictions y_i, the error is given by

$$\epsilon_i = y_i - x_i. \tag{2}$$

Mean error is defined as

$$\bar{\epsilon} = \frac{1}{n}\sum_{i=1}^{n}\epsilon_i. \tag{3}$$

$\bar{\epsilon}$ is a measure of bias; a positive value indicates that the model overpredicts on average, while a negative value indicates that the model underpredicts on average. An unbiased prediction will be indicated by $\bar{\epsilon}$ at or near zero.

The root-mean-square error (RMSE),

$$\mathrm{RMSE} = \sqrt{\frac{1}{n}\sum_{i=1}^{n}\epsilon_i^2}, \tag{4}$$

provides a measure of the average discrepancy between predictions and observations, independent of the sign of the error. RMSE is always positive and, like $\bar{\epsilon}$, has the same units as the input data. A smaller value for RMSE indicates a more accurate prediction.

Both mean error and RMSE are computed from a mean, and hence, their uncertainty can be computed using the formula for computing the uncertainty of a mean:

$$\sigma_{\mathrm{mean}} = \frac{\sigma}{\sqrt{n}}, \tag{5}$$

where n is the number of points, and σ is sample standard deviation of the points from which the mean is computed (Taylor, 1997). Taking σ as the standard deviation of all the points (std(x)), the uncertainty of RMSE is estimated by

$$\sigma_{\mathrm{RMSE}} = \sqrt{\frac{\mathrm{std}(\epsilon^2)}{\sqrt{n}}}, \tag{6}$$

and the uncertainty of mean error is estimated by

$$\sigma_{\bar{\epsilon}} = \frac{\text{std}(\epsilon)}{\sqrt{n}}. \tag{7}$$

All of the above metrics require a set of observations x_i and corresponding predictions y_i. Since the model is configured to produce output at specific times that may or may not coincide with the observations, linear interpolation of the model output is used to obtain values that correspond to the exact time of the observations. In the case of *Kp*, the model produces output at a much higher time resolution than the available observations, and this process results in a set of *Kp* predictions that correspond with the observations in terms of the number of values and in terms of the time range of the magnetometer data from which those values are derived.

Summarizing bias or accuracy with a single number provides a useful summary of a model's capabilities, but this single number can be misleading, particularly if the quantity being predicted has an asymmetric distribution. In the case of *Kp*, the pseudologarithmic scale complicates interpretation further. To get a more detailed picture of the model's predictive ability than is possible using mean error and RMSE, we compute probability density functions (PDFs) or distribution functions for each predicted quantity and its error. A PDF (or distribution function) of a quantity is a function that gives the relative likelihood that the variable will have a given value. Ideally, the distribution of the model values for a predicted quantity should be identical to the distribution of the observations for that quantity. Systematically biased predictions will result in a curve that is shifted right or left relative to the observations. When the shape of the PDF differs, this may indicate a tendency to overpredict or underpredict under a specific set of conditions. For the distribution of an error, the ideal case is a narrow, symmetric peak centered at zero. Bias in the model results in an off center or asymmetric peak in the error distribution. An inaccurate prediction is indicated by a broad peak.

For this paper we approximate PDFs using kernel density estimation (Parzen, 1962). This approximates the underlying PDF from a finite set of observations by smoothing with a kernel function, in this case a Gaussian. The bandwidth (the width of the Gaussian kernels) is determined for each PDF using Scott's rule (Scott, 2015). The specific implementation for the kernel density estimates is that of the SciPy software library (Jones et al., 2001).

3. Results

The mean error and RMSE of several predicted quantities were calculated for the entire month for each model configuration; these and their associated uncertainties are shown in Table 3. In addition to mean error and RMSE, we also give a normalized RMSE for each predicted quantity, which is computed by dividing the RMSE by the standard deviation of the observed values. By normalizing the RMSE values by the spread of the observational data, we obtain a unitless accuracy metric. This provides means to compare between RMSE values for disparate quantities. The normalized RMSE values seem to suggest that the model predicts *Kp* better than any other quantity. However, this is likely due to the fact that *Kp* is based on a 3 h maximum of magnetic field variations and is therefore insensitive to variations of shorter duration or magnitude. The other predicted quantities have 1 min time resolutions, so the prediction quality metrics for those quantities reflect errors in predicting high-frequency oscillations that are removed in the calculation of *Kp*. Note that all of the metrics in Table 3 are calculated for the entire month and, as a result, are likely dominated by the quiet time tendencies for each quantity.

The results are discussed in detail for each predicted quantity in sections 3.1–3.4, and differences between quiet and active periods are addressed where appropriate. The figures in the following sections use a common color scheme to identify results from the different model configurations. The SWPC configuration is shown in red, the high-resolution grid with RCM is shown in orange, and the high-resolution grid without RCM is shown in blue. Observations, where applicable, are shown as a thick, light blue curve.

3.1. *Kp*

The mean error and RMSE metrics for *Kp* are shown in Table 3. These values represent deviations on the pseudologarithmic *Kp* scale and hence are dimensionless. *Kp* predictions from the high-resolution configuration without RCM have the smallest RMSE (1.1), which indicates that these predictions have on average the best accuracy of the three model configurations, but the uncertainties in these RMSE values are large enough that

Table 3
Metrics for All Quantities and All Model Configurations, Given as the Value ± One Standard Error

	Model configuration		
Metric	SWPC	Hi-res w/ RCM	Hi-res w/o RCM
	Kp Metrics		
Mean error	0.68 ± 0.05	0.84 ± 0.06	−0.17 ± 0.07
RMSE	1.1 ± 0.3	1.3 ± 0.3	1.1 ± 0.4
Normalized RMSE	0.6 ± 0.2	0.8 ± 0.2	0.6 ± 0.2
	SYM-H Metrics		
Mean error (nT)	−7.36 ± 0.07	−3.99 ± 0.08	21.54 ± 0.09
RMSE (nT)	17 ± 2	18 ± 2	29 ± 3
Normalized RMSE	0.77 ± 0.09	0.86 ± 0.09	1.4 ± 0.1
	AL Metrics		
Mean error (nT)	71 ± 1	15 ± 1	123 ± 1
RMSE (nT)	250 ± 40	230 ± 40	270 ± 40
Normalized RMSE	0.9 ± 0.1	0.8 ± 0.1	1.0 ± 0.1
	CPCP Metrics		
Mean error (kV)	2.5 ± 0.2	14.9 ± 0.2	14.5 ± 0.2
RMSE (kV)	46 ± 10	47 ± 9	48 ± 9
Normalized RMSE	0.8 ± 0.2	0.8 ± 0.1	0.8 ± 0.1

the difference may not be significant. The high-resolution configuration without RCM also has the lowest bias with respect to *Kp* prediction, with a mean error of −0.20, indicating a slight underprediction. Both configurations with RCM have positive biases, indicating overprediction, and the biases are of greater magnitude than those for the configuration without RCM. Although the metrics seem to suggest that the configuration without RCM performs the best, they are misleading in this case as will be discussed later in this section when the distributions of *Kp* are examined in detail.

Figure 2a shows the probability distribution of *Kp* error for the three model configurations. The *Kp* error curve for the configuration without RCM is nearly centered about zero, indicating that the errors are relatively unbiased. The half width at half max of that curve is about 1, also consistent with the RMSE of 1.1 from Table 3. The *Kp* error curves for the SWPC configuration and the high resolution with RCM configuration are both centered to the right of zero. This indicates that these configurations tend to overpredict *Kp*, consistent with the positive mean errors shown in Table 3 for those configurations.

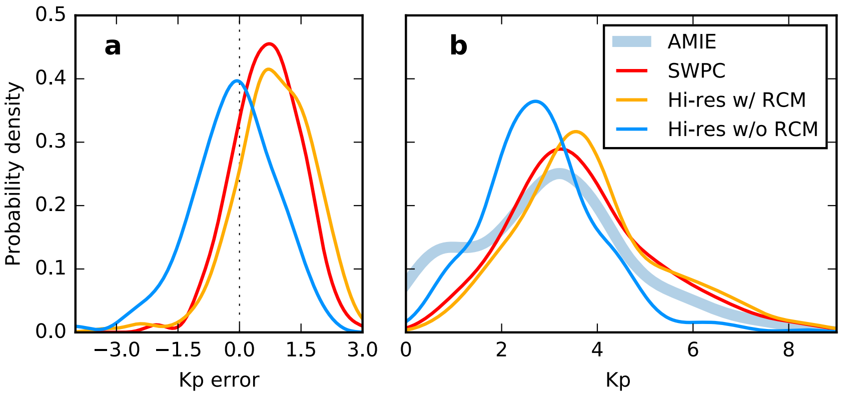

Figure 2. Probability density of (a) *Kp* error and (b) *Kp* itself for all model configurations during 1–31 January 2005. Distributions for the three model configurations are plotted as colored curves: SWPC in red, high-resolution with RCM in orange, and high-resolution without RCM in blue. Observations are shown as a thick, light blue curve.

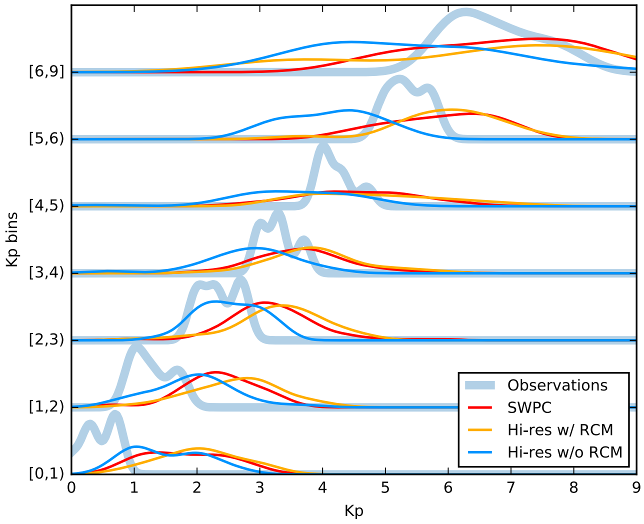

Figure 3. Probability density of *Kp* for observations and for all model configurations, binned by observed *Kp*. Tick labels on the *y* axis show the range of observed *Kp* values contained in each bin in the form $[Kp_{\min}, Kp_{\max})$. The light blue curve within each bin shows the probability density of *Kp* for the observations within that bin, while the colored curves show the distribution of predictions for each model corresponding to the times of the observations falling in the bin using the same color scheme as Figure 2.

The probability distributions of the actual *Kp* values are shown in Figure 2b. In addition to distributions obtained from the three model configurations, the observed distribution is shown as a thick, light blue curve. The observations have a mode at Kp $=$ 3.3. The two models that incorporate RCM (SWPC and high resolution with RCM) reproduce the observed distribution fairly closely, having peaks between 3 and 4 (reasonably close to the observed peak at Kp $=$ 3.3). However, they underpredict how often *Kp* values less than 2 will occur compared to the observations. The model configuration without RCM reproduces the observed distribution more closely in the $Kp = 0-2$ range than do the configurations with RCM. However, the *Kp* distribution from the without-RCM configuration also has its peak to the left of the observations, and indeed the entire distribution seems to be shifted to the left. The fact that the configuration without RCM agrees with the observations more closely in the low *Kp* range seems to be merely a side effect of this leftward shift. This means that the configuration without RCM produces more realistic quiet time *Kp* values but does so at the expense of accuracy during disturbed conditions.

Figure 3 shows distributions of *Kp* similar to the one in Figure 2b but broken down into bins covering specific ranges of observed *Kp*. The range of observed *Kp* values in each bin is labeled using the notation $[Kp_{\min}, Kp_{\max})$, indicating that the observed values in the bin start with $Kp_{\min}$ and go up to but do not include $Kp_{\max}$. For each bin, the model output is shown for the points in time corresponding to the observational data in that bin. The number of data points per bin ranges from 40 (in the $Kp \in [6,9)$ bin) to 200 (in the $Kp \in [3,4)$ bin). Note that the $Kp \in [6,9)$ bin covers a greater *Kp* range than the others; this was done to ensure the bin contains a sufficient number of points for analysis.

The binned distributions of Figure 3 provide a sense for how the model performance varies with the amount of geomagnetic activity. For the lowest *Kp* bins ($[0,1)$ and $[1,2)$), all of the models produce distributions shifted to the right compared with the observations, indicating a tendency to overpredict *Kp* during times of low activity. The overprediction appears to be least severe for the no-RCM configuration and most severe for the high-resolution grid with RCM. The high-resolution grid without RCM matches the observations fairly closely in the Kp $\in [2,3)$ bin but tends to underpredict for all higher *Kp* bins. The SWPC and Hi-res with RCM configurations continue to overpredict *Kp* up to the Kp $\in [3,4)$ bin. For the higher *Kp* values these configurations seem to produce relatively unbiased predictions.

Figure 4 shows the mean error for each of the *Kp* bins. The *x* axis shows the *Kp* bins using the same notation as Figure 3. The no-RCM configuration has positive mean error (indicating overprediction) for low *Kp*, but the mean error decreases with increasing *Kp*, reaching zero around $Kp = 2$ and having negative values thereafter (indicating underprediction). The two configurations with RCM (red and orange curves) also have a positive mean error for low *Kp*, with similar values to each other but greater magnitude (stronger bias) than that of the no-RCM configuration. The mean errors for these also decrease as *Kp* increases but at a slower rate than the no-RCM configuration. For the configurations with RCM the mean error remains positive up to $Kp = 5$ but turns negative for $Kp > 6$.

These results are similar to those of Glocer et al. (2016), which evaluated SWMF and several other models based on their predictions of local *K*. Glocer et al. (2016) did not include bias or accuracy metrics in their results, but in their supplemental data they provided distributions of predicted *K* for several values of observed *K*. From these, an unbiased prediction is apparent for observed K $=$ 4, an underprediction occurs for observed $K = 6$, and even greater underprediction for observed $K = 8$. Thus, the downward trend in bias is apparent as *K* increases in the Glocer et al. (2016) results, similar to the present work. The Glocer et al. (2016) results do not seem to show the positive bias that we see at lower values of *Kp*; this difference may be due to the Glocer et al. (2016) results being based on a study of storm events while our results include a considerable amount of quiet periods, as well as the difference in using individual magnetometer stations in that study versus the global *Kp* index in the present work.

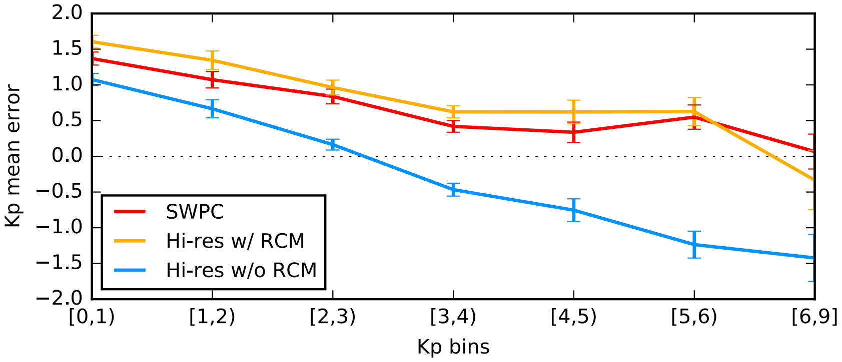

Figure 4. Mean error for each *Kp* bin. The ranges for each bin are denoted in the *x* axis labels in the form $[Kp_{\min}, Kp_{\max})$. The color scheme follows the previous figures. All the configurations overpredict low values of *Kp*, and the without-RCM configuration underpredicts the higher *Kp* values.

The model's ability to predict *Kp* during disturbed periods is notably improved with the addition of RCM, primarily during disturbed periods. This suggests that the differences between the model without RCM and those with (SWPC and Hi-res with RCM) are due primarily to differences in those current systems that are affected by the coupling with RCM, specifically the azimuthal currents that are modeled directly by RCM and the Region 2 field-aligned currents that are driven by inner magnetosphere pressure gradients affected by the coupling.

3.2. *SYM-H*

From the *SYM-H* results in Table 3, it is apparent that the two configurations using RCM (SWPC and Hi-res with RCM) predict *SYM-H* more accurately than the configuration without RCM. This is indicated by the comparatively low error (measured by RMSE) and bias (mean error closer to zero) relative to the configuration without RCM. The SWPC configuration predicts *SYM-H* with a slightly lower RMSE but a higher mean error than the high-resolution configuration with RCM. The configuration without RCM tends to overpredict *SYM-H* by 21.54 nT. The two configurations with RCM underpredict, but do so with a much lower magnitude (by a factor of 3–5) than the configuration with RCM.

Comparing these values of mean error and RMSE to the difference between *SYM-H* and similar indices gives a sense for whether the metrics indicate a good quality prediction. As mentioned earlier, Katus and Liemohn (2013) found discrepancies on the order of 9–11 nT between *SYM-H* and two similar indices. Therefore, *SYM-H* predictions with an RMSE of less than about 9–11 nT might be considered to be of good quality. The predictions from all three of our model configurations exceed 11 nT, but the two configurations with RCM exceed this threshold by only 55–65%, while the configuration without RCM exceeds it by 160%.

The probability distribution of *SYM-H* error (Figure 5a) shows a similar tendency as the metrics with regard to bias. The two runs with RCM appear largely similar to each other. Both are centered around zero (indicating an unbiased prediction) and have a half width at half maximum of about 15 nT. The run without RCM is centered around 15 nT, indicating a clear positive bias.

The distribution of *SYM-H* itself is shown in Figure 5b. The underlying cause for the positive bias of *SYM-H* from the no-RCM configuration is clearly apparent: It tends to produce *SYM-H* values near zero (as indicated by the high probability density at that point), while the observed distribution peaks around −20 nT and a long tail extending to −120 nT. The two configurations with RCM, on the other hand, produce a distribution that is largely similar to the observations.

A notable exception is the part of the distribution corresponding to *SYM-H* greater than 10 nT, where the configuration without RCM seems to produce a more realistic *SYM-H* distribution than the configurations with RCM. The observed distribution shows a small but significant probability for positive values of *SYM-H* going as high as 15 nT in Figure 5. The configuration without RCM appears to capture the outer part of this area (5–15 nT) fairly accurately. The two configurations with RCM, on the other hand, predict positive *SYM-H* values at a much lower rate than occur in the observations, as evidenced by the near-zero *SYM-H* probabilities between 5 and 15 nT for those configurations.

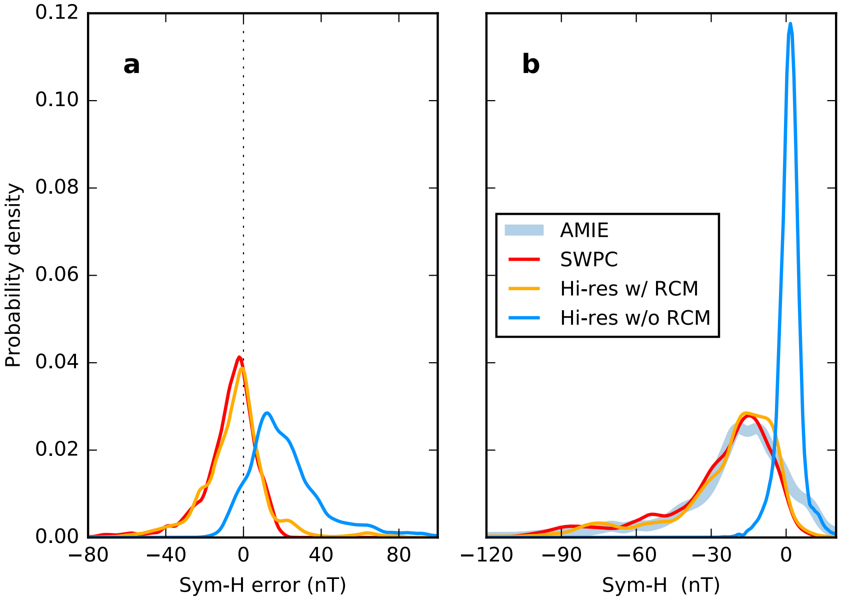

Figure 5. Probability density of (a) *SYM-H* error and (b) *SYM-H* itself for all model configurations. The color scheme follows the previous figures. The two configurations with RCM reproduce the observed *SYM-H* fairly well, while the one without RCM tends to produce *SYM-H* values near zero regardless of conditions.

Figure 6 shows time series of *SYM-H* during the storms on 7 and 21 January. For both of these storms, the configurations with RCM make reasonably good predictions of *SYM-H*, while the configuration without RCM produces very little *SYM-H* response except for some oscillations immediately following the initial disturbances. The two configurations with RCM, on the other hand, produce reasonably good approximations of the observed *SYM-H* response. These warrant further examination.

For the 7 January storm, the two configurations with RCM produce a minimum *SYM-H* of around −160 nT, while the observed *SYM-H* reached a minimum of −100 nT. Thus, the model *SYM-H* deviates from the observations by about 50% at the time of greatest disturbance. The models recover gradually over the course of about a day, at which point they are again close to the observed *SYM-H*. For the 21 January storm, the configurations with RCM produce a *SYM-H* curve that descends more sharply than the observations and rapidly reaches a minimum of −120 nT, again stronger than the observed minimum. In this case, however, the *SYM-H* from the configurations with RCM recovers rapidly, with the high-resolution configuration briefly becoming less negative than the observed *SYM-H* (from about 22:00 UT on 21 January to about 03:00 UT on 22 January) before descending again to match the observations. For the 21 January storm it took about 2 days (until 00:00 UT on 24 January) to recover, but in this case the model output (for the configurations with RCM) followed the observations closely throughout the recovery.

The tendency of the configurations with RCM (SWPC and Hi-Res w/ RCM) to miss positive *SYM-H* values previously noted in Figure 5 is apparent in both time series shown in Figure 6. In the case of the 21 January storm, a storm sudden commencement (SSC) is apparent. The configuration without RCM reproduces the observed *SYM-H* signature resulting from the SSC quite well, but the two configurations with RCM severely underpredict the magnitude of the SSC oscillations. A possible explanation for this is that the inner magnetosphere currents produced by RCM counteract the effects of magnetopause currents to a greater degree than occur in reality. This reduces the influence of such currents on the surface magnetic fields and in turn the frequency and magnitude of positive *SYM-H* values as seen in Figure 5.

The time series plots of *SYM-H* show considerable improvement in *SYM-H* predictions over some earlier results such as Ganushkina et al. (2010) in which SWMF predicted *SYM-H* with approximately correct magnitudes but with an approximately 6 h delay compared to the observed *SYM-H*. A similar improvement can be seen in other work such as Liemohn et al. (2013) and in some (though arguably not all) of the *Dst* time series plots in Rastätter et al. (2013).

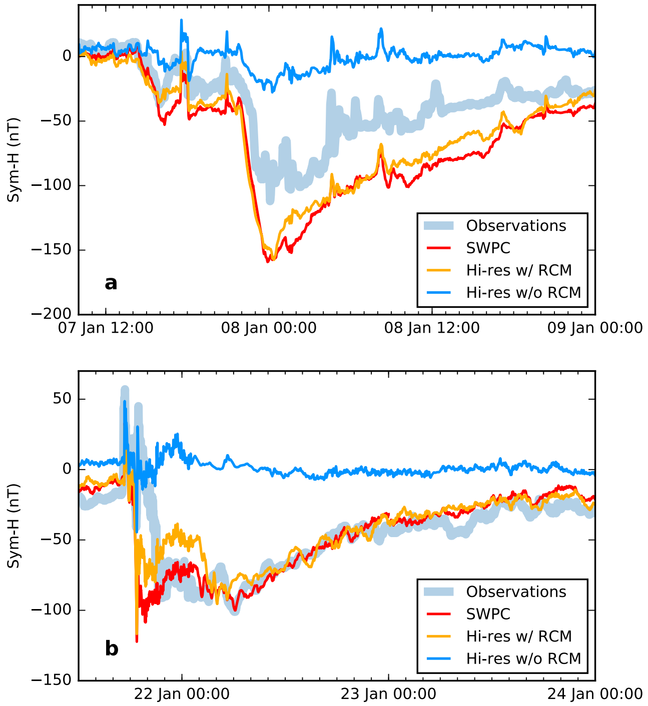

Figure 6. *SYM-H* time series for the storms on (a) 7 January and (b) 21 January. The color scheme is the same as the previous figures. The model configurations with RCM produce stronger (by 20–50%) *SYM-H* responses than the observations, while the configuration without RCM produces little response to the storms.

The stark difference in *SYM-H* predictions with and without the RCM component highlights the importance of the inner magnetosphere model in producing realistic ring current dynamics. The inner magnetosphere model can also, through coupling with the MHD solver, affect midtail currents to which *SYM-H* is sensitive, as evidenced by increased tail stretching in MHD models when coupling to an inner magnetosphere model is used (e.g., Pembroke et al., 2012; Welling et al., 2015). That SWMF predicts *Dst* (similar to *SYM-H*) better when a ring current model is used has been shown previously in Rastätter et al. (2013). Changing the MHD grid resolution, on the other hand, seems to have relatively little effect on *SYM-H*.

3.3. *AL*

Table 3 shows that the mean error in *AL* is positive for all configurations, indicating a tendency to overpredict *AL*. Note that *AL* has negative values during times of high activity, so overprediction of *AL* implies underprediction of geomagnetic activity. Of all the model configurations, the high-resolution grid with RCM exhibits the lowest mean error for *AL*. The RMSE values are comparable for all three model configurations, falling within the uncertainty bounds of each other. The RMSE values for all of the models are much larger than the mean error, suggesting that random errors rather than bias are the main contributor to the RMSE values.

The distribution of error in *AL* is shown in Figure 7a. Because the distribution is characterized by a long tail, it is plotted on a logarithmic scale. All three configurations peak around zero, but the wings of the distributions are asymmetric, with higher probabilities in the positive direction than the negative. This asymmetry is apparently responsible for the positive biases shown in the *AL* section of Table 3. The asymmetry is most severe for the high-resolution configuration with RCM, and least severe for the high-resolution configuration with RCM. The fact that the curves peak near zero suggests that the model produces fairly unbiased *AL* predictions most of the time, but the asymmetry indicates an occasional tendency toward overprediction.

The distribution of the *AL* values themselves is shown in Figure 7b. All of the model configurations peak just to the left of zero, similar to the observations. At the same time, they underpredict the probabilities of the more negative *AL* values. The high-resolution grid with RCM underpredicts less severely than the other configurations. As a result, the high-resolution grid with RCM comes somewhat closer to reproducing the observed distribution. The underprediction of the frequency of strongly negative values is probably the main cause of the biases apparent in the *AL* section of Table 3 and Figure 7a. It is worth noting that positive *AL* values

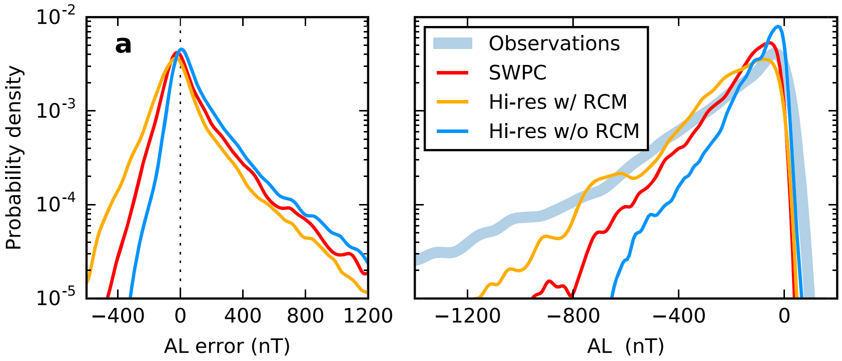

Figure 7. Probability density of (a) *AL* error and (b) *AL* itself for observations and for all model configurations. The color scheme follows the previous figures. The distribution is shown on a logarithmic scale due to the importance of the wings of the distribution. All three model configurations capture the overall shape of the distribution but underpredict the probability of large negative values.

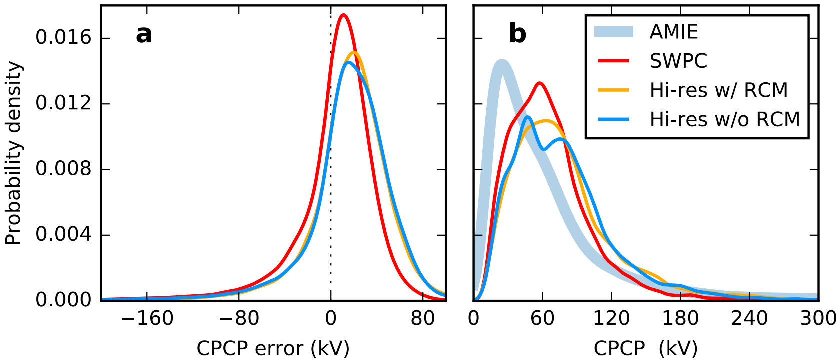

Figure 8. Probability densities of CPCP error relative to the (a) AMIE model and of (b) CPCP itself for all model configurations. The color scheme is the same as the previous figures. These plots show that all of the model configurations overpredict CPCP.

are underpredicted by all of the models and less severely by the configuration without RCM. This may be related to the results for *Kp*, where the no-RCM configuration performed better than the others during times of low activity.

The fact that the error curves peak near zero (Figure 7a) suggests that the model configurations all tend to produce realistic quiet time conditions. The wings in the error distributions suggest less accurate predictions during times of higher activity. At the same time, all the model configurations underpredict how often the strongest negative *AL* values will occur (Figure 7b). This implies that the model produces a weaker westward electrojet current during disturbed periods than occurs in the observations. Since the westward electrojet is often associated with substorms (Akasofu & Yoshida, 1966), this suggests that the model underpredicts the magnitude of substorm-related field-aligned currents.

3.4. CPCP

The errors for CPCP are calculated relative to the AMIE model (Richmond, 1992; Richmond & Kamide, 1988). In the CPCP section of Table 3, all three SWMF configurations show positive mean error for CPCP compared to AMIE, indicating overprediction. The SWPC configuration overpredicts only slightly, while the two high-resolution configurations overpredict more significantly. All three configurations have an RMSE that well exceeds the mean error, indicating that the errors in CPCP are not dominated by a systematic bias in one particular direction.

Probability distributions of CPCP error are shown in Figure 8a. All of the error distributions have peaks to the right of zero (around 20–30 kV), consistent with the positive mean errors reported for CPCP in Table 3. The peaks are centered 5–15 kV higher than the mean errors shown in Table 3, perhaps due to the long, thin tail of negative errors found in all three distributions.

The distribution of CPCP itself is shown in Figure 8b. The probability density of AMIE outputs (thick, light blue curve) peaks around 25 kV, while the model configurations all peak around 50–60 kV. This results in the models overestimating CPCP on average, as was seen in Table 3. The CPCP distributions obtained from all three models have half widths at half max of around 45 kV, slightly greater than the width of the observed distribution.

Figure 9 shows distributions of CPCP, binned by observed CPCP. The range of observed CPCP values in each bin is labeled using the notation [$\mathrm{CPCP}_{\mathrm{min}}$, $\mathrm{CPCP}_{\mathrm{max}}$), much like Figure 3. From these it is immediately clear that all three models overpredict CPCP during quiet times but underpredict during active times. This pattern is similar to what occurred for *Kp* except that the configuration without RCM no longer stands out from the others.

Discrepancies between modeled and observed CPCP could be attributed to a number of possible underlying causes, including strength and location of field-aligned currents, ionospheric conductivity, and ionospheric outflow. The field-aligned current structure and conductivity both affect the potential through Ohm's Law, $\mathbf{J} = \sigma\mathbf{E}$, where the potential is proportional to the current and inversely proportional to conductivity. Thus, overprediction of the potential (which occurs primarily during quiet time) indicates either overprediction of field-aligned current strength or underprediction of the conductivity. Conversely, underprediction of the

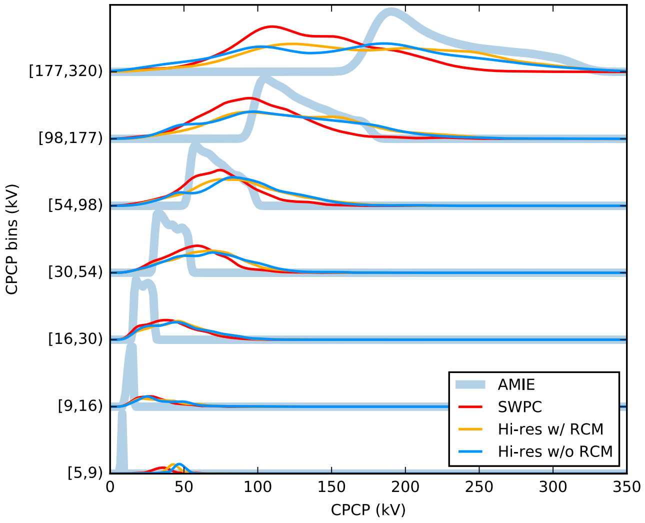

Figure 9. Probability density of CPCP for observations and for all model configurations, binned by observed CPCP. Tick labels on the *y* axis show the range of observed CPCP values contained in each bin in the form [$\mathrm{CPCP}_{\mathrm{min}}$, $\mathrm{CPCP}_{\mathrm{max}}$). Probability distributions corresponding to each bin are plotted following the same color scheme used in previous figures. The model tends to overpredict CPCP during quiet times but underpredict during the most active times.

potential (which occurs primarily during active times) indicates either underprediction of the field-aligned current strengths or overprediction of the conductivity.

The conductivity connection may also indicate a discrepancy in rate of outflow from the ionospheric boundary. CPCP has been shown to decrease as heavy ion outflow from the ionosphere increases (Welling & Zaharia, 2012; Winglee et al., 2002), so the fact that the models overpredict CPCP could be an indication that the model is underpredicting such outflow. This could be addressed through tuning of the inner boundary condition parameters, but such tuning is complicated by the fact that the outflow is itself dependent on CPCP (Winglee, 2000; Welling & Liemohn, 2014) and is likely to affect other aspects of the model such as tail dynamics, ring current, and the *SYM-H* values that are predicted (Kronberg et al., 2014; Welling & Liemohn, 2016). First-principles based models of ionospheric outflow provide an alternative, but at present they are too computationally expensive for long-period runs such as those described in the present work.

4. Discussion

The relatively good accuracy achieved by the model implies a reasonably good model of the magnetospheric currents that affect the various observed quantities, including the dependency of those currents on solar wind driving and other aspects of the dynamics. Furthermore, the similarities between the results for the two highest resolution runs suggest that the model configuration is near grid convergence with regard to the predicted quantities examined in this paper. A notable exception is the *AL* index, where a larger difference can be seen. This could be due to the high-latitude current structures to which *AL* is sensitive, which may require a higher resolution in order to be fully resolved.

It is worth noting that the high-resolution configuration with RCM differs from the SWPC configuration not only in the grid but also its use of the Young et al. (1982) empirical composition model in the coupling between BATS-R-US and RCM. This means that we cannot definitively attribute differences in predictions from those two configurations to the difference in grid resolution. Another limitation of these results is that the data come from a single 1 month period, so any dependence of the results on season, such as those found by Juusola et al. (2014), or solar cycle will not be apparent.

The fact that *SYM-H* is predicted more accurately when RCM is used is expected because RCM simulates current systems to which *SYM-H* is sensitive. These same current systems are likely responsible for improving the *Kp* distribution as well. *Kp* can be directly influenced by the current systems that affect *SYM-H*, particularly during times when the strength of the currents are rapidly changing. At the same time, the Region 2 field-aligned currents, to which *Kp* is also sensitive, are driven in part by the kinds of inner magnetosphere currents that are modeled by RCM. This has been shown theoretically by Vasyliunas (1970) and demonstrated using an inner magnetosphere model by Zheng et al. (2006, 2008). The mean error and RMSE metrics for *Kp* seem to suggest a detrimental effect of RCM, but this is due to the quiet time overprediction *Kp* being masked by an overall reduction in the magnitude of *Kp* due to the lack of a ring current.

Since the model overpredicts both *Kp* and CPCP during quiet times, it seems that there may be a common cause (or causes) behind the discrepancies in those quantities. Both *Kp* and CPCP are sensitive to middle- and high-latitude ionospheric state and dynamics (particle precipitation, conductivity, and currents). One possible underlying cause of these discrepancies is the model of ionospheric conductivity, which directly affects CPCP and affects *Kp* through the current structure. In the present model, the ionospheric conductivity is obtained from a number of empirical relationships. The range of validity for these empirical relationships can easily be exceeded during execution of an MHD model under realistic conditions and, in fact, was exceeded during the month in question. Welling et al. (2017) identify the range of validity for these models in terms of solar wind electric field to be from −1.84 mV/m to 2.30 mV/m. Solar wind electric field is defined in that paper as $u_x B_z$, where u_x is the solar wind velocity in GSM coordinates and B_z is the IMF magnetic field in the GSM *z* direction. $u_x B_z$ for January 2005 ranged from −28.6 mV/m to 25.2 mV/m, roughly an order of magnitude greater than the valid range listed in Welling et al. (2017). The observational data used to construct the empirical conductivity model used in RIM came from solar flux observations from 1985 to 1990 and magnetometer data from a 1 month period of January 1997 (Moen & Brekke, 1993; Ridley et al., 2004b). Construction of a more comprehensive empirical model by including more recent data would certainly be possible. Such an improved conductance model might result in better representation of auroral current systems and, in turn, indices and other observable quantities that are sensitive to them.

Like the present paper, Wiltberger et al. (2017) found 0.25 R_E to be sufficient resolution for resolving certain aspects of magnetospheric dynamics. They compared field-aligned currents for a 1 month run of the Lyon-Fedder-Mobarry (LFM) MHD model and compared the results with the Weimer (2005) empirical model. They presented results using three different grid resolutions, the finest of which had cell sizes between 0.25 and 0.5 R_E in the inner magnetosphere, similar to the SWPC grid used in the present work. They found that the relationship between field-aligned currents and CPCP was very similar between the two highest-resolution grids and concluded that the model was approaching a common solution at those resolutions. However, the results they reported were based on time averages for the entire run, so underresolved transient features might not affect the results significantly. The indications in the present work are that the greatest magnitudes of the *AL* index are underpredicted, and these correspond with transient phenomena.

Wiltberger et al. (2017) also found that LFM underpredicted field-aligned current strength and overpredicted CPCP compared to the Weimer (2005) model. This could be explained by an underprediction of ionospheric conductivity in that model. Analyzing field-aligned current strength in SWMF might shed some light on the problem of ionospheric conductivity, but such an analysis is beyond the scope of the present paper. Nonetheless, the results of the present work, like Wiltberger et al. (2017), suggest that ionospheric conductivity is an area for improvement.

5. Conclusions

This work shows the strengths and limitations of the SWMF with regard to prediction of geomagnetic indices and CPCP. By testing a 1 month period with three different model configurations, we have accumulated a sufficient quantity of data to make statistical comparisons with observations under a variety of conditions.

We find that the model does an excellent job of predicting the *SYM-H* index. With RCM turned on, the model predicts *SYM-H* with RMSE values of 17–18 nT, only 50–60% larger than the observational uncertainty for that index. The model predicts the *Kp* index well during storm conditions, with absolute mean errors of less than 1 for *Kp* values above 3. During quiet time though, it consistently overpredicts *Kp*, with all configurations overpredicting by at least 1 *Kp* unit on average. An overprediction of quiet time activity is also apparent in the model's prediction of CPCP, with mean errors between 2.5 and 14.9 kV. The model tends to underpredict the magnitude of the *AL* index, with mean errors between 15 and 230 nT.

Of the quantities assessed in this paper, the model performs best at predicting *SYM-H*, and least well at predicting *AL*. That the model predicts *SYM-H* poorly without RCM is an expected exception to this. The model's relatively poor performance in predicting *AL* indicates problems in capturing the structure of auroral zone currents. A better model of ionospheric conductivity would probably be the most effective way to improve these in the near term, although better predictions of dynamics affecting the field-aligned current structure are needed if the auroral zone observations are to be predicted to a high degree of accuracy. Depending on what changes are made, such improvements may also reduce the problem of overpredicting *Kp* during quiet time as well, since *Kp* is also sensitive to auroral zone dynamics.

Increasing the grid resolution compared with the SWPC grid had relatively little effect on prediction quality. For all four predicted quantities, the model's predictive accuracy, measured by RMSE, changed by insignificant amounts, as indicated by the error bounds of each RMSE value. There are some indications that the increased grid resolution may have improved the model's prediction of the more extreme values attained by the *AL* index, however. This implies that the auroral currents during disturbed periods are improved by the increased grid resolution.

Unlike the grid resolution, the presence or absence of an inner magnetosphere model has a dramatic effect on the *SYM-H* results, with the distribution of *SYM-H* taking a notably different shape and width when RCM was turned off, and a resulting change in RMSE that far exceeded the uncertainty bound (29 nT without RCM versus 18 nT with RCM). The *Kp* and *AL* indices are also affected by the use of RCM, though to a lesser degree than the *SYM-H* index. Like the *SYM-H* index, the predictive skill for the *AL* index was improved by the use of RCM, with RMSE increasing from 230 nT to 270 nT when RCM was turned off. RMSE proved to be somewhat misleading as a measure of accuracy for *Kp*. RMSE decreased notably when RCM was turned off, which ordinarily would indicate better accuracy. However, a careful examination of the data set reveals that the accuracy only improved during relatively quiet periods ($Kp \leq 2$), while the accuracy during the most disturbed intervals was noticeably worse. CPCP was the only quantity not affected significantly by the use of the inner magnetosphere model, with only a very small change in RMSE when RCM was turned off.

The data sets produced for this paper can be utilized for a number of possible follow-on projects. The MHD solution can be used to reproduce spacecraft observations, which will enable an assessment of the model's ability to predict magnetic fields in the inner magnetosphere, and locations of the bow shock and magnetopause. As mentioned in the previous section, the field-aligned current structure can be analyzed in detail in order to determine what aspects of the field-aligned currents the model is able to capture. Finally, the model output can be analyzed to identify signatures of substorms, in order to assess how well the model reproduces their timing and dynamics.

It may be useful to conduct additional work like this covering other time periods. This would make it possible to assess variations depending on season or solar cycle. The resulting data sets could also be analyzed in combination, which would produce results with increased statistical significance and enable more detailed statistical analysis.

Appendix A: Model Configuration Details

A1. MHD Solver

For all of the runs in this paper we use BATS-R-US (Powell et al., 1999) to solve the ideal MHD equations. The flux scheme is Sokolov's Local Artificial Wind flux (see Sokolov et al., 2002) and a Koren's third-order limiter (Koren, 1993) with beta = 1.2. Cross sections of the two MHD grids are shown in Figure A1. These cross sections are in the *X*-*Z* plane through the origin; the grids are symmetric such that *Y*-*Z* cuts through the origin would look identical. Both are Cartesian grids in GSM coordinates, with the cell size varied using adaptive mesh refinement. The outer boundaries form a cube 256 Earth radii (R_E) in width. The grids are offset in the x direction so that they extends 32 R_E sunward of the Earth and 224 R_E tailward. In the y and z directions the grids are centered around the Earth, extending 128 R_E from the Earth along each of those axes. An inflow boundary condition populated with time-dependent solar wind data is used on the boundary located at $x = 32\ R_E$, while the opposite face (at $x = -224\ R_E$) uses an outflow boundary condition. The remaining outer boundaries use a zero-gradient boundary condition.

While the two grids are identical in their overall extent, their resolutions differ significantly. The SWPC grid (Figure A1, left) has cell sizes ranging from 8 R_E at the outflow boundaries to 0.25 R_E within a 16 R_E diameter cube surrounding the Earth. The cell size of the high-resolution grid (Figure A1, right) varies from 8 R_E at the outflow boundaries to 0.125 R_E near the Earth. The refined regions are the same as those used in Welling and Ridley (2010). A 1 R_E cell size is used in a region around the x axis extending from the inflow boundary to 112 R_E downtail, while the near-tail region from 8 to 20 R_E downtail is resolved to 0.25 R_E. The minimum cell size occurs within an 8 R_E wide cube surrounding the Earth, from which a 2.5 R_E sphere is excluded from the MHD grid; this region is modeled through coupling to the ionospheric model described in the next section. The SWPC grid contains around 1 million cells, while the high-resolution grid contains 1.9 million cells.

A2. Inner Magnetosphere

In the inner magnetosphere, transport by gradient and curvature drift becomes more important to the plasma motion, making the ideal MHD approximation inaccurate there (Heinemann & Wolf, 2001). We model this region using the Rice Convection Model (RCM). By averaging out the gyro and bounce motion, this model treats the inner magnetosphere plasma as a fluid that drifts across field lines.

Unlike the MHD solver, the RCM breaks the plasma population into bins according to an energy invariant, and each energy invariant is treated as a separate fluid. In addition, oxygen, hydrogen, and electrons are treated as separate species. Since the MHD solver is being run in single-fluid mode, the coupling between the two codes must divide the MHD fluid into hydrogen and oxygen. The operational model used by SWPC accomplishes this by using a fixed ratio of 10% oxygen and 90% hydrogen by number density. However, we found that with the higher-resolution grid this configuration resulted in poorer quality *SYM-H* predictions than with the lower

Acknowledgments
Thanks to Ruth Skoug of Los Alamos National Laboratory for providing solar wind data from the Advanced Composition Explorer (ACE) satellite to cover gaps in the publicly available Level 2 data sets. Thanks to World Data Center Kyoto for providing observed values for the *SYM-H* index, the NOAA NGDC for providing observed values for the *Kp* index, and the NASA Goddard Spaceflight Center for their OMNI and CDAWeb tools that provide access to a variety of data sets. For the ground magnetometer data we gratefully acknowledge Intermagnet; USGS, Jeffrey J. Love; CARISMA, PI Ian Mann; CANMOS; the S-RAMP Database, PI K. Yumoto, and K. Shiokawa; the SPIDR database; AARI, PI Oleg Troshichev; the MACCS program, PI M. Engebretson, Geomagnetism Unit of the Geological Survey of Canada; GIMA; MEASURE, UCLA IGPP, and Florida Institute of Technology; SAMBA, PI Eftyhia Zesta; 210 Chain, PI K. Yumoto; SAMNET, PI Farideh Honary; the institutes who maintain the IMAGE magnetometer array, PI Liisa Juusola; PENGUIN; AUTUMN, PI Martin Connors; DTU Space, PI Rico Behlke; South Pole and McMurdo magnetometer, PI's Louis J. Lanzarotti, and Alan T. Weatherwax; ICESTAR; RAPIDMAG; PENGUIn; British Artarctic Survey; McMac, PI Peter Chi; BGS, PI Susan Macmillan; Pushkov Institute of Terrestrial Magnetism, Ionosphere and Radio Wave Propagation (IZMIRAN); GFZ, PI Juergen Matzka; MFGI, PI B. Heilig; IGFPAS, PI J. Reda; University of L'Aquila, PI M. Vellante; and SuperMAG, PI Jesper W. Gjerloev. This research was conducted as part of the Space Hazards Induced near Earth by Large, Dynamic Storms (SHIELDS) project, funded by the U.S. Department of Energy through the LANL/LDRD-DR program under contract DE-AC52-06NA25396. S. Morley was supported by the U.S. Department of Energy Laboratory Directed Research and Development (LDRD) project award 20170047DR. N. Ganushkina thanks the International Space Science Institute (ISSI) in Bern, Switzerland, for the support of the international teams on "Analysis of Cluster Inner Magnetosphere Campaign Data, in Application to the Dynamics of Waves and Wave-Particle Interaction within the Outer Radiation Belt," and "Ring Current Modeling: Uncommon Assumptions and Common Misconceptions." The research of N. Ganushkina leading to these results was partly funded by the European Union's Horizon 2020 research and innovation program under grant agreement 637302 PROGRESS. Support for N. Ganushkina at Michigan was provided by research grants

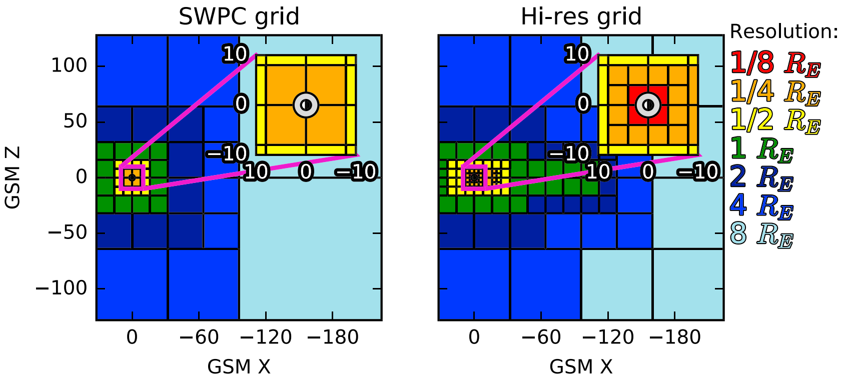

Figure A1. *X-Z* cuts showing cell sizes in the two MHD grids. (left) The grid used for the SWPC configuration (minimum cell size of 0.25 R_E. (right) The higher-resolution grid used for the other two runs (minimum cell size of 0.125 R_E).

resolution grid. We were able to address this problem by replacing the fixed oxygen to hydrogen ratio with one computed using the empirical plasma sheet composition model from Young et al. (1982). The Young et al. (1982) model gives relative quantities of oxygen and hydrogen as a function of $F_{10.7}$ and *Kp*. In our implementation, $F_{10.7}$ values are provided through an input file, and *Kp* is obtained from the MHD solver. The results presented in this paper use the fixed ratios of 10% oxygen and 90% hydrogen for the SWPC configuration and the Young et al. (1982) model for the high-resolution with RCM configuration.

A3. Ionospheric Electrodynamics

The Ridley Ionosphere Model (RIM) calculates ionospheric parameters on a height-integrated basis. This model is described in Ridley and Liemohn (2002) and Ridley et al. (2004a). It receives field-aligned current values from the MHD solver and, from these, calculates conductance and electric potential. The potential values are then passed back to the inner magnetosphere and MHD models, where they are used to determine the velocity tangent to the inner boundary (the velocity normal to the boundary is set to zero) (Welling & Liemohn, 2014). As discussed in Welling and Liemohn (2016), the ionospheric boundary is of crucial importance to the overall dynamics of the magnetospheric dynamics. While more sophisticated models exist to model the interaction through this boundary, most are either too computationally costly (such as the Polar Wind Outflow Model, Glocer et al., 2007) or lack a fully tested coupling to an MHD model.

References

Akasofu, S.-I., & Yoshida, S. (1966). Growth and decay of the ring current and the polar electrojets. *Journal of Geophysical Research*, *71*(1), 231–240. https://doi.org/10.1029/JZ071i001p00231

Anderson, B. J., Korth, H., Welling, D. T., Merkin, V. G., Wiltberger, M. J., Raeder, J., … ... (2017). Comparison of predictive estimates of high-latitude electrodynamics with observations of global-scale Birkeland currents. *Space Weather*, *15*, 352–373. https://doi.org/10.1002/2016SW001529

Bartels, J., Heck, N. H., & Johnston, H. F. (1939). The three-hour-range index measuring geomagnetic activity. *Terrestrial Magnetism and Atmospheric Electricity*, *44*(4), 411–454. https://doi.org/10.1029/TE044i004p00411

Borovsky, J. E. (2012). The effect of sudden wind shear on the Earth's magnetosphere: Statistics of wind shear events and CCMC simulations of magnetotail disconnections. *Journal of Geophysical Research*, *117*, A06224. https://doi.org/10.1029/2012JA017623

Bristow, W. A., Greenwald, R. A., Shepherd, S. G., & Hughes, J. M. (2004). On the observed variability of the cross-polar cap potential. *Journal of Geophysical Research*, *109*, A02203. https://doi.org/10.1029/2003JA010206

Cash, M. D., Witters Hicks, S., Biesecker, D. A., Reinard, A. A., de Koning, C. A., & Weimer, D. R. (2016). Validation of an operational product to determine L1 to Earth propagation time delays. *Space Weather*, *14*, 93–112. https://doi.org/10.1002/2015SW001321

Cramer, W. D., Raeder, J., Toffoletto, F. R., Gilson, M., & Hu, B. (2017). Plasma sheet injections into the inner magnetosphere: Two-way coupled openGGCM-RCM model results. *Journal of Geophysical Research: Space Physics*, *122*, 5077–5091. https://doi.org/10.1002/2017JA024104

Crooker, N. U., Lyon, J. G., & Fedder, J. A. (1998). MHD model merging with IMF By: Lobe cells, sunward polar cap convection, and overdraped lobes. *Journal of Geophysical Research*, *103*(A5), 9143–9151. https://doi.org/10.1029/97JA03393

Davis, T. N., & Sugiura, M. (1966). Auroral electrojet activity index *AE* and its universal time variations. *Journal of Geophysical Research*, *71*(3), 785–801. https://doi.org/10.1029/JZ071i003p00785

De Zeeuw, D. L., Gombosi, T. I., Groth, C. P. T., Powell, K. G., & Stout, Q. F. (2000). An adaptive MHD method for global space weather simulations. *IEEE Transactions on Plasma Science*, *28*, 1956–1965.

Dubyagin, S., Ganushkina, N., Kubyshkina, M., & Liemohn, M. (2014). Contribution from different current systems to SYM and ASY midlatitude indices. *Journal of Geophysical Research: Space Physics*, *119*, 7243–7263. https://doi.org/10.1002/2014JA020122

Facskó, G., Honkonen, I., Živković, T., Palin, L., Kallio, E., Ågren, K., … Milan, S. (2016). One year in the Earth's magnetosphere: A global MHD simulation and spacecraft measurements. *Space Weather*, *14*, 351–367. https://doi.org/10.1002/2015SW001355

Gannon, J., & Love, J. (2011). USGS 1-min *Dst* index. *Journal of Atmospheric and Solar-Terrestrial Physics*, *73*(2-3), 323–334. https://doi.org/10.1016/j.jastp.2010.02.013

from NASA (NNX14AF34G and NNX17AI48G). Full output from the three-model runs presented in this paper can be found at the following URLs: http://vmr.engin.umich.edu/Model/_swmf_mag/plot?run=Jan2005_SWPC, http://vmr.engin.umich.edu/Model/_swmf_mag/plot?run=Jan2005_Hi-res_w_RCM, and http://vmr.engin.umich.edu/Model/_swmf_mag/plot?run=Jan2005_Hi-res_wo_RCM.

Ganushkina, N. Y., Liemohn, M. W., Kubyshkina, M. V., Ilie, R., & Singer, H. J. (2010). Distortions of the magnetic field by storm-time current systems in Earth's magnetosphere. *Annales Geophysicae*, *28*(1), 123–140. https://doi.org/10.5194/angeo-28-123-2010

Ganushkina, N. Y., Pulkkinen, T. I., Kubyshkina, M. V., Singer, H. J., & Russell, C. T. (2004). Long-term evolution of magnetospheric current systems during storms. *Annales Geophysicae European Geosciences Union*, *22*(4), 1317–1334.

Gjerloev, J. W. (2012). The SuperMAG data processing technique. *Journal of Geophysical Research*, *117*, A09213. https://doi.org/10.1029/2012JA017683

Glocer, A., Fok, M., Meng, X., Tóth, G., Buzulukova, N., Chen, S., & Lin, K. (2012). CRCM + BATS-R-US two way coupling. *Journal of Geophysical Research*, *118*, 1635–1650. https://doi.org/10.1002/jgra.50221

Glocer, A., Gombosi, T. I., Tóth, G., Hansen, K. C., Ridley, A. J., & Nagy, A. (2007). Polar wind outflow model: Saturn results. *Journal of Geophysical Research*, *112*, A01304. https://doi.org/10.1029/2006JA011755

Glocer, A., Rastätter, L., Kuznetsova, M., Pulkkinen, A., Singer, H. J., Balch, C., … Wing, S. (2016). Community-wide validation of geospace model local K-index predictions to support model transition to operations. *Space Weather*, *14*, 469–480. https://doi.org/10.1002/2016SW001387

Groth, C., De Zeeuw, D. L., Gombosi, T., & Powell, K. (2000). Global 3D MHD simulation of a space weather event: CME formation, interplanetary propagation, and interaction with the magnetosphere. *Journal of Geophysical Research*, *105*, 25,053–25,078.

Guild, T. B., Spence, H. E., Kepko, E. L., Merkin, V., Lyon, J. G., Wiltberger, M., & Goodrich, C. C. (2008). Geotail and LFM comparisons of plasma sheet climatology: 1. Average values. *Journal of Geophysical Research*, *113*, A04216. https://doi.org/10.1029/2007JA012611

Heinemann, M., & Wolf, R. A. (2001). Relationships of models of the inner magnetosphere to the rice convection model. *Journal of Geophysical Research*, *106*(A8), 15,545–15,554.

Hirsch, C. (2007). *Numerical computation of internal and external flows: The fundamentals of computational fluid dynamics*. Oxford: Butterworth-Heinemann.

Huang, C.-L., Spence, H. E., Singer, H. J., & Hughes, W. J. (2010). Modeling radiation belt radial diffusion in ULF wave fields: 1. Quantifying ULF wave power at geosynchronous orbit in observations and in global MHD model. *Journal of Geophysical Research*, *115*, A06215. https://doi.org/10.1029/2009JA014917

Iyemori, T. (1990). Storm-time magnetospheric currents inferred from mid-latitude geomagnetic field variations. *Journal of Geomagnetism and Geoelectricity*, *42*(11), 1249–1265. https://doi.org/10.5636/jgg.42.1249

Janhunen, P., Palmroth, M., Laitinen, T., Honkonen, I., Juusola, L., Facskó, G., & Pulkkinen, T. I. (2012). The GUMICS-4 global {MHD} magnetosphere-ionosphere coupling simulation. *Journal of Atmospheric and Solar-Terrestrial Physics*, *80*, 48–59. https://doi.org/10.1016/j.jastp.2012.03.006

Jones, E., Oliphant, T., & Peterson, P. (2001). SciPy: Open source scientific tools for Python, Accessed March 06, 2017.

Juusola, L., Facskó, G., Honkonen, I., Janhunen, P., Vanhamäki, H., Kauristie, K., … Viljanen, A. (2014). Statistical comparison of seasonal variations in the GUMICS-4 global MHD model ionosphere and measurements. *Space Weather*, *12*, 582–600. https://doi.org/10.1002/2014SW001082

Kalegaev, V. V., Ganushkina, N. Y., Pulkkinen, T. I., Kubyshkina, M. V., Singer, H. J., & Russell, C. T. (2005). Relation between the ring current and the tail current during magnetic storms. *Annales Geophysicae*, *23*(2), 523–533.

Katus, R. M., & Liemohn, M. W. (2013). Similarities and differences in low- to middle-latitude geomagnetic indices. *Journal of Geophysical Research: Space Physics*, *118*, 5149–5156. https://doi.org/10.1002/jgra.50501

Koren, B. (1993). A robust upwind discretisation method for advection, diffusion and source terms. In C. Vreugdenhil & B. Koren (Eds.), *Numerical methods for advection-diffusion problems* (pp. 117). Braunschweig: Vieweg.

Kress, B. T., Hudson, M. K., Looper, M. D., Albert, J., Lyon, J. G., & Goodrich, C. C. (2007). Global MHD test particle simulations of $>$10 MeV radiation belt electrons during storm sudden commencement. *Journal of Geophysical Research*, *112*, A09215. https://doi.org/10.1029/2006JA012218

Kronberg, E. A., Iannis, M. A.-a., Delcourt, D. C., Grigorenko, E. E., Kistler, L. M., Kuzichev, I. V., … Zelenyi, L. M. (2014). Circulation of heavy ions and their dynamical effects in the magnetosphere: Recent observations and models charge energy mass experiment extreme ultraviolet radiation. *Space Science Reviews*, *184*, 173–235. https://doi.org/10.1007/s11214-014-0104-0

Liemohn, M. W., De Zeeuw, D. L., Ganushkina, N. Y., Kozyra, J. U., & Welling, D. T. (2013). Magnetospheric cross-field currents during the January 6–7, 2011 high-speed stream-driven interval. *Journal of Atmospheric and Solar-Terrestrial Physics*, *99*, 78–84. https://doi.org/10.1016/j.jastp.2012.09.007

Liemohn, M. W., Kozyra, J. U., Thomsen, M. F., Roeder, J. L., Lu, G., Borovsky, J. E., & Cayton, T. E. (2001). Dominant role of the asymmetric ring current in producing the stormtime Dst*. *Journal of Geophysical Research*, *106*(A6), 10,883–10,904. https://doi.org/10.1029/2000JA000326

Lockwood, M., & Morley, S. K. (2004). A numerical model of the ionospheric signatures of time-varying magnetic reconnection: I. Ionospheric convection. *Annales Geophysicae*, *22*(1), 73–91.

Lopez, R., Lyon, J., Wiltberger, M., & Goodrich, C. (2001). Comparison of global MHD simulation results with actual storm and substorm events. *Advances in Space Research*, *28*(12), 1701–1706. https://doi.org/10.1016/S0273-1177(01)00535-X

Lyon, J., Fedder, J., & Mobarry, C. (2004). The Lyon-Fedder-Mobarry (LFM) global MHD magnetospheric simulation code. *Journal of Atmospheric and Solar-Terrestrial Physics*, *66*, 1333–1350.

Maltsev, Y. (2004). Points of controversy in the study of magnetic storms. *Space Science Reviews*, *110*(3/4), 227–277. https://doi.org/10.1023/B:SPAC.0000023410.77752.30

Mayaud, P. N. (1980). *Derivation, meaning, and use of geomagnetic indices*. Washington, DC: American Geophysical Union. https://doi.org/10.1002/9781118663837

McComas, D. J., Bame, S. J., Barker, P., Feldman, W. C., Phillips, J. L., Riley, P., & Griffee, J. W. (1998). *Solar Wind Electron Proton Alpha Monitor (SWEPAM) for the advanced composition explorer* (pp. 563–612). Dordrecht, Netherlands: Springer. https://doi.org/10.1007/978-94-011-4762-0_20

Milan, S. E. (2004). Dayside and nightside contributions to the cross polar cap potential: Placing an upper limit on a viscous-like interaction. *Annales Geophysicae*, *22*(10), 3771–3777. https://doi.org/10.5194/angeo-22-3771-2004

Moen, J., & Brekke, A. (1993). The solar flux influence of quiet-time conductances in the auroral ionosphere. *Geophysical Research Letters*, *20*, 971–974.

Morley, S. K. (2007). *7th Australian space science conference proceedings* (pp. 118–129). Australia: National Space Society of Australia Ltd.

Morley, S., Koller, J., Welling, D., Larsen, B., & Niehof, J. (2014). SpacePy: Python-Based Tools for the Space Science Community, Astrophysics Source Code Library.

Morley, S. K., Rouillard, A. P., & Freeman, M. P. (2009). Recurrent substorm activity during the passage of a corotating interaction region. *Journal of Atmospheric and Solar-Terrestrial Physics*, *71*(10), 1073–1081. https://doi.org/10.1016/j.jastp.2008.11.009

Morley, S. K., Welling, D. T., Koller, J., Larsen, B. A., Henderson, M. G., & Niehof, J. (2011). *SpacePy — A Python-based library of tools for the space sciences*. Paper presented at Proceedings of the 9th Python in Science Conference (pp. 39–45). Austin, TX.

Ngwira, C. M., Pulkkinen, A., Leila Mays, M., Kuznetsova, M. M., Galvin, A. B., Simunac, K., … Glocer, A. (2013). Simulation of the 23 July 2012 extreme space weather event: What if this extremely rare CME was earth directed? *Space Weather*, *11*, 671–679. https://doi.org/10.1002/2013SW000990

Ngwira, C. M., Pulkkinen, A., Kuznetsova, M. M., & Glocer, A. (2014). Modeling extreme "Carrington-type" space weather events using three-dimensional global MHD simulations. *Journal of Geophysical Research: Space Physics*, *119*, 4456–4474. https://doi.org/10.1002/2013JA019661

Ogino, T., Walker, R. J., & Ashour-Abdalla, M. (1992). A global magnetohydrodynamic simulation of the magnetosheath and magnetosphere when the interplanetary magnetic field is northward. *IEEE Transactions on Plasma Science*, *20*(6), 817–828. https://doi.org/10.1109/27.199534

Ohtani, S., Nosé, M., Rostoker, G., Singer, H., & Lui, A. (2001). Storm-substorm relationship: Contribution of the tail current. *Journal of Geophysics*, *106*, 21,199–21,209.

Palmroth, M., Pulkkinen, T. I., Janhunen, P., & Wu, C.-C. (2003). Stormtime energy transfer in global MHD simulation. *Journal of Geophysical Research*, *108*, 1048. https://doi.org/10.1029/2002JA009446

Parzen, E. (1962). On estimation of a probability density function and mode. *Annals of Mathematical Statistics*, *33*(3), 1065–1076. https://doi.org/10.1214/aoms/1177704472

Pembroke, A., Toffoletto, F., Sazykin, S., Wiltberger, M., Lyon, J., Merkin, V., & Schmitt, P. (2012). Initial results from a dynamic coupled magnetosphere-ionosphere-ring current model. *Journal of Geophysical Research*, *117*, A02211. https://doi.org/10.1029/2011JA016979

Powell, K., Roe, P., Linde, T., Gombosi, T., & De Zeeuw, D. L. (1999). A solution-adaptive upwind scheme for ideal magnetohydrodynamics. *Journal of Computational Physics*, *154*, 284–309.

Pulkkinen, A., Rastätter, L., Kuznetsova, M., Hesse, M., Ridley, A., Raeder, J., … Chulaki, A. (2010). Systematic evaluation of ground and geostationary magnetic field predictions generated by global magnetohydrodynamic models. *Journal of Geophysical Research*, *115*, A03206. https://doi.org/10.1029/2009JA014537

Pulkkinen, A., Rastätter, L., Kuznetsova, M., Singer, H., Balch, C., Weimer, D., … Weigel, R. (2013). Community-wide validation of geospace model ground magnetic field perturbation predictions to support model transition to operations. *Space Weather*, *11*, 369–385. https://doi.org/10.1002/swe.20056

Raeder, J., Berchem, J., & Ashour-Abdalla, M. (1998). The geospace environment modeling grand challenge: Results from a global geospace circulation model. *Journal of Geophysical Research*, *103*(A7), 14,787 — 14,797. https://doi.org/10.1029/98JA00014

Raeder, J., McPherron, R., Frank, L., Kokubun, S., Lu, G., Mukai, T., … Slavin, J. (2001). Global simulation of the Geospace environment modeling substorm challenge event. *Journal of Geophysical Research*, *106*, 381–395.

Rastätter, L., Kuznetsova, M. M., Glocer, A., Welling, D., Meng, X., Raeder, J., … Gannon, J. (2013). Geospace environment modeling 2008–2009 challenge: Dst index. *Space Weather*, *11*, 187–205. https://doi.org/10.1002/swe.20036

Rastätter, L., Kuznetsova, M. M., Vapirev, A., Ridley, A., Wiltberger, M., Pulkkinen, A., … Singer, H. J. (2011). Geospace environment modeling 2008–2009 challenge: Geosynchronous magnetic field. *Space Weather*, *9*, S04005. https://doi.org/10.1029/2010SW000617

Richmond, A. D. (1992). Assimilative mapping of ionospheric electrodynamics. *Advances in Space Research*, *12*, 59.

Richmond, A. D., & Kamide, Y. (1988). Mapping electrodynamic features of the high-latitude ionosphere from localized observations: Technique. *Journal of Geophysical Research*, *93*(A6), 5741. https://doi.org/10.1029/JA093iA06p05741

Ridley, A., Gombosi, T., & Dezeeuw, D. (2004a). Ionospheric control of the magnetosphere: Conductance. *Annales Geophysicae*, *22*, 567–584. https://doi.org/10.5194/angeo-22-567-2004

Ridley, A., Gombosi, T., & Dezeeuw, D. (2004b). Ionospheric control of the magnetosphere: Conductance. *Annales Geophysicae*, *22*, 567–584.

Ridley, A. J., & Liemohn, M. W. (2002). A model-derived storm time asymmetric ring current driven electric field description. *Journal of Geophysical Research*, *107*(A8), 2002. https://doi.org/10.1029/2001JA000051

Ridley, A. J., Gombosi, T. I., De Zeeuw, D. L., Clauer, C. R., & Richmond, A. D. (2003). Ionospheric control of the magnetosphere: Thermospheric neutral winds. *Journal of Geophysical Research*, *108*, 1328. https://doi.org/10.1029/2002JA009464

Rostoker, G. (1972). Geomagnetic indices. *Reviews of Geophysics*, *10*(4), 935–950. https://doi.org/10.1029/RG010i004p00935

Sazykin, S. Y. (2000). Theoretical studies of penetration of magnetospheric electric fields to the ionosphere (Ph.D. thesis), Utah State University, Logan, Utah.

Scott, D. W. (2015). *Multivariate density estimation: Theory, practice, and visualization* (2nd edn.). New York: John Wiley & Son.

Sokolov, I., Timofeev, E. V., Sakai, J., & Takayama, K. (2002). Artificial wind — A new framework to construct simple and efficient upwind shock-capturing schemes. *Journal of Computational Physics*, *181*, 354–393. https://doi.org/10.1006/jcph.2002.7130

Tapping, K. F. (2013). The 10.7cm solar radio flux ($F_{10.7}$). *Space Weather*, *11*, 394–406. https://doi.org/10.1002/swe.20064

Taylor, J. (1997). *An introduction to error analysis: The study of uncertainties in physical measurements*. Sausalito, CA: University Science Books.

Thomsen, M. F. (2004). Why Kp is such a good measure of magnetospheric convection. *Space Weather*, *2*, S11004. https://doi.org/10.1029/2004SW000089

Toffoletto, F., Sazykin, S., Spiro, R., & Wolf, R. (2003). Inner magnetospheric modeling with the Rice Convection Model. *Space Science Reviews*, *107*, 175–196.

Tóth, G., Sokolov, I. V., Gombosi, T. I., Chesney, D. R., Clauer, C., Zeeuw, D. L. D., … ... (2005). Space weather modeling framework: A new tool for the space science community. *Journal of Geophysical Research*, *110*, A12226. https://doi.org/10.1029/2005JA011126

Tóth, G., van der Holst, B., Sokolov, I. V., De Zeeuw, D. L., Gombosi, T. I., Fang, F., … Opher, M. (2012). Adaptive numerical algorithms in space weather modeling. *Journal of Computational Physics*, *231*(3), 870–903. https://doi.org/10.1016/j.jcp.2011.02.006

Vasyliunas, V. M. (1970). *Mathematical models of magnetospheric convection and its coupling to the ionosphere* (pp. 66–71). Netherlands: Springer. https://doi.org/10.1007/978-94-010-3284-1_6

Wanliss, J. A., & Showalter, K. M. (2006). High-resolution global storm index: Dst versus $SYM\text{-}H$. *Journal of Geophysical Research*, *111*, A02202. https://doi.org/10.1029/2005JA011034

Weimer, D. R. (2004). Correction to "Predicting interplanetary magnetic field (IMF) propagation delay times using the minimum variance technique". *Journal of Geophysical Research*, *109*, A12104. https://doi.org/10.1029/2004JA010691

Weimer, D. R. (2005). Improved ionospheric electrodynamic models and application to calculating joule heating rates. *Journal of Geophysical Research*, *110*, A05306. https://doi.org/10.1029/2004JA010884

Weimer, D. R., & King, J. H. (2008). Improved calculations of interplanetary magnetic field phase front angles and propagation time delays. *Journal of Geophysical Research*, *113*, A01105. https://doi.org/10.1029/2007JA012452

Weimer, D. R., Ober, D. M., Maynard, N. C., Collier, M. R., McComas, D. J., Ness, N. F., … Watermann, J. (2003). Predicting interplanetary magnetic field (IMF) propagation delay times using the minimum variance technique. *Journal of Geophysical Research*, *108*, 1026. https://doi.org/10.1029/2002JA009405

Welling, D. T., & Liemohn, M. W. (2014). Outflow in global magnetohydrodynamics as a function of a passive inner boundary source. *Journal of Geophysical Research: Space Physics*, *119*, 2691–2705. https://doi.org/10.1002/2013JA019374

Welling, D. T., & Liemohn, M. W. (2016). The ionospheric source of magnetospheric plasma is not a black box input for global models. *Journal of Geophysical Research: Space Physics*, *121*, 5559–5565. https://doi.org/10.1002/2016JA022646

Welling, D. T., & Ridley, A. J. (2010). Validation of SWMF magnetic field and plasma. *Space Weather*, *8*, S03002. https://doi.org/10.1029/2009SW000494

Welling, D. T., & Zaharia, S. G. (2012). Ionospheric outflow and cross polar cap potential: What is the role of magnetospheric inflation? *Geophysical Research Letters*, *39*, L23101. https://doi.org/10.1029/2012GL054228

Welling, D. T., Anderson, B. J., Crowley, G., Pulkkinen, A. A., & Rastätter, L. (2017). Exploring predictive performance: A reanalysis of the geospace model transition challenge. *Space Weather*, *15*, 192–203. https://doi.org/10.1002/2016SW001505

Welling, D. T., Jordanova, V. K., Glocer, A., Toth, G., Liemohn, M. W., & Weimer, D. R. (2015). The two-way relationship between ionospheric outflow and the ring current. *Journal of Geophysical Research: Space Physics*, *120*, 4338–4353. https://doi.org/10.1002/2015JA021231

Wiltberger, M., Rigler, E., Merkin, V., & Lyon, J. (2017). Structure of high latitude currents in magnetosphere-ionosphere models. *Space Science Reviews*, *206*, 575–598. https://doi.org/10.1007/s11214-016-0271-2

Winglee, R. (2000). Mapping of ionospheric outflows into the magnetosphere for varying IMF conditions. *Journal of Atmospheric and Solar-Terrestrial Physics*, *62*, 527–540.

Winglee, R. M., Chua, D., Brittnacher, M., Parks, G. K., & Lu, G. (2002). Global impact of ionospheric outflows on the dynamics of the magnetosphere and cross-polar cap potential. *Journal of Geophysical Research*, *107*(A9), 1237. https://doi.org/10.1029/2001JA000214

Wolf, R. A., Harel, M., Spiro, R. W., Voigt, G., Reiff, P. H., & Chen, C. K. (1982). Computer simulation of inner magnetospheric dynamics for the magnetic storm of July 29, 1977. *Journal of Geophysical Research*, *87*, 5949–5962.

Wu, C. C., Walker, R. J., & Dawson, J. M. (1981). A three dimensional MHD model of the Earth's magnetosphere. *Geophysical Research Letters*, *8*(5), 523–526. https://doi.org/10.1029/GL008i005p00523

Young, D. T., Balsiger, H., & Geiss, J. (1982). Correlations of magnetospheric ion composition with geomagnetic and solar activity. *Journal of Geophysical Research*, *87*(A11), 9077–9096. https://doi.org/10.1029/JA087iA11p09077

Yu, Y., & Ridley, A. (2008). Validation of the space weather modeling framework using ground-based magnetometers. *Space Weather*, *6*, S05002. https://doi.org/10.1029/2007SW000345

Yu, Y., Ridley, A. J., Welling, D. T., & Tóth, G. (2010). Including gap region field-aligned currents and magnetospheric currents in the MHD calculation of ground-based magnetic field perturbations. *Journal of Geophysical Research*, *115*, A08207. https://doi.org/10.1029/2009JA014869

Yu, Y., Jordanova, V., Welling, D., Larsen, B., Claudepierre, S. G., & Kletzing, C. (2014). The role of ring current particle injections: Global simulations and Van Allen Probes observations during 17 March 2013 storm. *Geophysical Research Letters*, *41*, 1126–1132. https://doi.org/10.1002/2014GL059322

Zhang, B., Lotko, W., Wiltberger, M., Brambles, O., & Damiano, P. (2011). A statistical study of magnetosphere-ionosphere coupling in the Lyon-Fedder-Mobarry global MHD model. *Journal of Atmospheric and Solar-Terrestrial Physics*, *73*(5-6), 686–702. https://doi.org/10.1016/j.jastp.2010.09.027

Zhang, J., Liemohn, M. W., De Zeeuw, D. L., Borovsky, J. E., Ridley, A. J., Toth, G., … Wolf, R. A. (2007). Understanding storm-time ring current development through data-model comparisons of a moderate storm. *Journal of Geophysical Research*, *112*, A04208. https://doi.org/10.1029/2006JA011846

Zheng, Y., Lui, A. T. Y., Fok, M.-C., Anderson, B. J., Brandt, P. C., Immel, T. J., & Mitchell, D. G. (2006). Relationship between Region 2 field-aligned current and the ring current: Model results. *Journal of Geophysical Research*, *111*, A11S06. https://doi.org/10.1029/2006JA011603

Zheng, Y., Lui, A. T., Fok, M.-C., Anderson, B. J., Brandt, P. C., & Mitchell, D. G. (2008). Controlling factors of Region 2 field-aligned current and its relationship to the ring current: Model results. *Advances in Space Research*, *41*, 1234–1242. https://doi.org/10.1016/j.asr.2007.05.084